Evaluation of light atmospheric plume inversion methods using synthetic XCO2 satellite images to compute Paris CO2 emissions

Alexandre Danjou, Grégoire Broquet, Jinghui Lian, Francois-Marie Breon, Thomas Lauvaux

Remote Sensing of Environment 305 (2024) 113900

Contents lists available at ScienceDirect

Remote Sensing of Environment

journal homepage: www.elsevier.com/locate/rse

Evaluation of light atmospheric plume inversion methods using synthetic XCO_2 satellite images to compute Paris CO_2 emissions

Alexandre Danjou [a,*], Grégoire Broquet [a], Jinghui Lian [a,b], François-Marie Bréon [a], Thomas Lauvaux [a,c]

[a] Laboratoire des Sciences du Climat et de l'Environnement, LSCE/IPSL, CEA-CNRS-UVSQ, Université Paris-Saclay, 91198 Gif-sur-Yvette, France
[b] Origins.earth, Suez Group, 92040 Paris, La Défense, France
[c] Groupe de Spectrométrie Moléculaire et Atmosphérique (GSMA), UMR CNRS 7331, Université de Reims-Champagne-Ardennes, 51687 Reims, France

ARTICLE INFO

Edited by: Dr. Menghua Wang

Keywords:
CO2
Urban emissions
Mass-balance methods
Gaussian plumes
OCO-3
OCO-2
GHGs

ABSTRACT

There is a growing interest in estimating urban CO_2 emission from space-borne imagery of XCO_2. Here, we evaluate computationally-light methods (mass-balance approaches and inversions of Gaussian plume models) for estimating urban emissions with Paris, France, as an example. This evaluation is based on the application of those methods to synthetic high-resolution images of the XCO_2 field in the Paris area, either with hypothetical 165km × 200km images at 1km × 1km resolution or using actual ≈2km resolution sampling by OCO-2 and OCO-3. Our work quantifies and analyzes the different sources of error when applying these methods and the corresponding pre-processing steps in detail. We start with ideal test cases with perfect knowledge of the background concentration field and of the driving effective wind and area of the plume from Paris, and without measurement noise in the images. Then we introduce sources of errors associated to these components of the estimation problem step by step. With the best configuration for the different methods, and when accounting for these sources of errors, we obtain total errors in the emission estimates with little bias (<10% of the actual emissions) and a relatively large interquartile range (≈75% of the actual emissions). Overall, the different methods that are tested show similar skills for the emission calculation. The two main sources of uncertainty are the estimates of the background concentration and of the effective wind speed. The error statistics are sensitive to meteorological conditions, mainly to the spatial variability of the wind direction, and to the variability of the background XCO_2 field. These sources of error and the results' sensitivity to background and wind field variabilities are theoretically shared by the complex atmospheric inversion methods currently used to quantify urban emissions and the computationally-light methods tested here. Therefore, these conclusions can be extended to the general problem of quantifying urban CO_2 emissions from XCO_2 imagery. Using OCO-2-like or OCO-3-like samplings, rather than hypothetical 200 km wide images at 1 km resolution, increases the random uncertainty in the emission estimates but not the biases in these estimates.

1. Introduction

Urban areas encompass more than half of the global population, hence a significant fraction of fossil fuel emissions (UNDESA, 2018). Many cities across the globe have decided to take their part in GHG emission reduction (e.g., Covenant of Mayors: https://www.covenantofmayors.eu). To assess their reduction pathway, city governments and climate policy makers monitor their emissions (both direct -e.g., from vehicle traffic in the cities- and indirect -e.g., from road transport or power plants outside their boundaries supplying the cities) through self-reported inventories (SRIs). However, a recent comparison between published SRIs of US cities and the Vulcan inventory by Gurney et al. (2021) showed large discrepancies between these two datasets, despite a geographic alignment of the city boundaries and emission sectors, gases, and scope. This comparison pointed out the inaccuracy of the emission evaluation in most SRIs. In principle, quantifying CO_2 emissions of cities via atmospheric data could provide accurate information to support the cities' SRIs. Studies such as Bréon et al. (2015) or Lauvaux et al. (2016) have initiated the assessment of the potential of urban ground-based sensors network to quantify CO_2 emissions at city scale. However, the

* Corresponding author.
E-mail address: alexandre.danjou@lsce.ipsl.fr (A. Danjou).

https://doi.org/10.1016/j.rse.2023.113900
Received 26 September 2023; Accepted 4 November 2023
Available online 6 March 2024

required network density (Kort et al., 2013), the cost of the sensors, as well as the calibration and maintenance protocols, make the wide deployment of this solution difficult (Wu et al., 2016). In principle, satellites, with their global coverage, can support quantifying the emissions from a larger number of cities and thus the verification of mitigation trajectories at large-scale (Janssens-Maenhout et al., 2020). However, inverting city emissions using satellite data requires adequate observation sampling and raises specific challenges (Ciais et al., 2015). Current missions dedicated to monitoring CO_2 use passive instruments measuring the absorption of reflected sunlight in the short wave infrared (SWIR). Such measurements are used to derive the column-average dry air mole fraction of CO_2 (XCO_2). There is currently a lack of missions providing observations supporting the estimate of urban emissions. The Orbiting Carbon Observatory missions (OCO-2/3) of NASA/JPL offers the most suitable dataset to assess the potential of quantifying urban emission from space (Chevallier et al., 2022; Lei et al., 2021; Wu et al., 2020; Ye et al., 2017; Zheng et al., 2020).

OCO-2's main goal is the large-scale monitoring of CO_2 natural fluxes. It has a narrow swath on the ground (<10km) and provides measurements at high resolution: at 1.25 km × 2.5 km in nadir mode (Eldering et al., 2017). At such a high resolution, OCO-2 captures local enhancements of CO_2 concentrations when the satellite swath crosses a significant mass of CO_2 emitted by a city or a large point source downwind to this source, i.e., the plume from this source. Different types of methods can be used to estimate the emission of the source based on the detected enhancements. The observed enhancements can be compared to the theoretical enhancements given by a transport model, and thus used to rescale the source emission in this model. The transport model can be a computationally expensive Eulerian or Lagrangian model (Wu et al., 2018; Ye et al., 2017), or a simpler model such as a Gaussian plume model (Krings et al., 2011). Alternatively, direct flux integration techniques, generally called "mass-balance methods", can be used. These rely on direct multiplication of the enhancements by the wind to derive an estimate of the source emission (Zheng et al., 2020). Hereafter, all these methods are called inversion methods, as they analyze the consequence of the release of XCO_2 in the atmosphere i.e. the local XCO_2 enhancements, to quantify the cause of this release, i.e. the source emission.

However, OCO-2 captures only a small portion of the city plumes when crossing them, as its swath is relatively narrow. Indeed, the typical length of these plumes is one to a few hundred kilometers. Using images that are wide enough to cover the whole sources and a large part of their plumes should improve the accuracy of emission estimates (Santaren et al., 2021). Indeed, a larger image width provides a broader view of the plumes' shape and of the background fields, and more pixels to analyze the plume XCO_2 enhancement. It thus increases the potential to detect pixels covered by the urban plume, i.e., with significant XCO_2 enhancement due to the city emissions. Furthermore, it increases the potential to filter or limit the impact of observational noise and background concentration variations, which are due to the meteorological conditions or to other CO_2 sources and sinks. Future satellite missions will provide high-resolution observations within large swaths (Santaren et al., 2020). Despite its moderate extent of about 80km × 80km, the Snapshot Area Map (SAM) mode of the OCO-3 instrument, onboard the International Space Station (Eldering et al., 2019), is the first attempt to deliver images of plumes from cities and industrial plants at ≈2km resolution using the pointing capability of the instrument. Thus OCO-3 is considered a demonstrator of the future high-resolution imagers like the CO2M constellation (Kuhlmann et al., 2021). This study analyzes the potential of such imagery for monitoring CO_2 emissions from urban centers.

Past studies have examined the potential to monitor urban emissions with XCO_2 large-swath imagers using inversion methods which relied on traditional Bayesian frameworks and complex mesoscale Eulerian or Lagrangian atmospheric transport models (Broquet et al., 2018; Pillai et al., 2016). These studies focused primarily on the propagation of errors associated with satellite data into emission estimates. In such inversion frameworks, tranport model errors are often represented by unbiased random noise without spatial correlation (Rayner et al., 2019). Only a few inversion systems offer the opportunity to adjust the atmospheric transport in parallel with the emissions due to the complexity implied by such a concept (Liu et al., 2012). However, due to uncertainties in the meteorological fields, in the emission vertical injection profile and in vertical motion at high spatial and temporal resolutions, atmospheric transport can be responsible for significant mismatches between simulated and observed plumes in terms of location, shape, or magnitude of the corresponding XCO_2 enhancements. For example, Ye et al. (2017) pointed out mismatches between the locations of the XCO_2 enhancements corresponding to city plumes simulated by the Weather Research and Forecasting (WRF)-Chem model (Skamarock et al., 2008) and observed by OCO-2. Consequently, transport errors introduce large uncertainties and even biases in emissions estimates. Inversion of simplified transport models (like Gaussian models) or direct flux integration techniques relying on pre-calculated wind fields, which are studied here, are less computationally expensive (Zheng et al., 2020) and offer a more flexible representation of atmospheric transport than mesoscale models. In particular, their parameters can be easily adapted to fit the observed plume shape and direction. For example, Nassar et al. (2017) adjusted the direction of their Gaussian plume model to analyze the XCO_2 enhancements in OCO-2 data corresponding to power plants and quantify the corresponding emissions.

The low computational cost of these methods is critical for processing a large number of images. In October 2022, OCO-3 provided >3000 SAMs with >1000 valid pixels over large cities and industrial sources. Future missions such as CO2M should provide many more images of plumes than OCO-3. The wide application of local scale atmospheric inversion approaches using Eulerian or Lagrangian models on these datasets should be hampered by the cost for setting-up, testing and running these models for each source. The light computational approaches studied here can process large amounts of plume images, enabling the monitoring of many cities across the globe at a high temporal frequency and over multiple years (Chevallier et al., 2020).

In this study, we assess the potential of XCO_2 images to quantify urban CO_2 emissions whith the most commonly-used computationally-light methods. Our evaluation uses synthetic observations over the Paris region, simulated based on a high-resolution inventory of fossil fuel emissions (Lian et al., 2022), biogenic fluxes from a simplified vegetation model, and an Eulerian mesoscale atmospheric transport model. We compare three variants of Gaussian plume model inversions (GP) to several direct flux integration techniques: Integrated Mass Enhancement (IME), Source Pixel (SP), and Cross-Sectional (CS) methods. In a general way, these methods rely on the assumption of stationarity of the emissions and meteorology (wind), even though some of them can provide some flexibility to account for temporal variations in the emissions. Some studies have applied such methods to quantify urban CO_2 emissions based on pseudo XCO_2 images (Kuhlmann et al., 2020) or based on observed XCO_2 plume cross-sections from OCO-2 (Chevallier et al., 2020; Reuter et al., 2019; Zheng et al., 2020). However, these methods have never been fully evaluated or compared using various configuration options. We aim to maximize their performances by highlighting the optimal methods and parameters under various meteorological conditions. Using experiments with synthetic data where the true emission and concentrations are known, our assessment of the different methods and configurations rely on the comparison of their emission estimates to the true emissions. We focus on a specific area, the Paris metropolitan region, considering three observation modes. Our main observation mode assumes a 1 km resolution imagery over an area of 165km × 200 km. The two other observation modes correspond to OCO-2 tracks and OCO-3 SAMs.

Varon et al. (2018) evaluated the potential of the methods studied here to estimate stationary CH_4 emissions from industrial point sources based on XCH_4 images at <1 km resolution. However, the requirements

for the estimation of urban CO_2 emission based on XCO_2 images, with a sampling similar to CO2M, can differ from those highlighted by Varon et al. (2018). The urban emissions have a spatial distribution which generates plumes that are much wider and complex than the plumes from point sources. Current XCO_2 images have a broader coverage than XCH_4 images in Varon et al. (2018) but also a coarser spatial resolution. Therefore, we re-evaluate the computationally light inversion methods for the monitoring of urban XCO_2 emissions based on current to near term XCO_2 images. We also examine the individual pre-processing steps associated to these methods: mainly the computation of the effective wind speed (i.e., the average wind driving the location and shape of the XCO_2 plume) and the detection in the XCO_2 image of the targeted plume enhancements and of the corresponding XCO_2 background.

Section 2 presents the model and the pseudo data used for our tests; Section 3 describes the different configurations for the emission estimation methods, which combine the inversion methods and their pre-processing steps. Section 4 evaluates the results given by the different configurations and highlights the optimal ones. Finally, Section 5 discusses the results, the potential errors not considered, and the perspectives for the light emission estimation methods.

2. Idealized simulation and experiment protocol

2.1. General description of the experiments

We evaluate the emission estimation methods based on a large ensemble of pseudo-images of XCO_2 centered on Paris, covering the full domain of simulation or corresponding to the actual XCO_2 sampling from the OCO missions. The application of the estimation methods aims at retrieving the emissions from the core urban area of Paris at the time of the satellite overpass. This area covers Paris and most of its suburban area (see Section 2.2 for a precise definition of these geographical areas). The atmospheric plumes that can be detected and analyzed in satellite images over the region correspond better to the core urban area than to the areas within the different administrative boundaries. The core urban area is thus a suitable target for the emission estimation. The city center is taken as the point of coordinates 48° 51′12″ N 2° 20′55″ E.

The Paris metropolitan area is located in a vast sedimentary basin with limited topography, about 150 km away from the coast of the English Channel. The region encompasses about 10% of the national CO_2 emissions (sources: Origins.earth inventory, see Section 2.2 and CITEPA, see https://www.citepa.org/fr/2021-co2/, last access March 17th, 2022) and 11% of the French population (6.8 million inhabitants) over a limited surface (0.1% of France surface). Paris is quite isolated from other major emitters. Due to its high population density and relatively compact urbanisation, the urban area of Paris generates a narrow plume that does not overlap other major urban plumes. Therefore, the plumes from Paris are easy to detect compared to those from other large metropolitan areas (Santaren et al., 2021). However, the XCO_2 enhancements due to the urban emissions simulated in our experiments hardly exceed 1 ppm locally, i.e., they are generally smaller than the random noise of current XCO_2 spaceborne instruments.

The idealized XCO_2 data used in this study are simulated from December 1st 2019 to April 30th 2020 using the WRF-Chem model. For each day during this period, we extract the resulting XCO_2 hourly fields between 10:00 and 16:00 (local time) to simulate XCO_2 images for each observation mode. We conduct an ensemble of emission estimations on each of the corresponding 1064 pseudo-images (152 days × 7 h) for each observation mode. The timing for the extraction of the images varies in order to increase the number of weather conditions represented in the ensemble of tests, but restrained to daytime only. To date, all space-borne instruments dedicated to monitoring CO_2 concentrations collect passive measurements of the reflected sunlight and thus provide daytime observations. While sun-synchronous missions like OCO-2 (or CO2M in the future) provide images at fixed local time, OCO-3 takes its SAMs at local times varying between 10:00 and 18:00 (Eldering et al., 2019).

2.2. Model configuration

We use high-resolution simulations of hourly atmospheric CO_2 concentrations by WRF-Chem V3.9.1 based on the configuration described in Lian et al. (2019, 2021, 2022). The WRF model configuration uses a one-way nesting across three domains (D01, D02, and D03) at 25, 5, and 1 km horizontal resolution respectively, in which the innermost domain (D03, shown in Fig. 1) covers the Ile-de-France (IdF) region. IdF corresponds to an administrative area which includes the Paris core urban area and its surrounding, extending beyond Paris' suburbs. The surface physics schemes in our simulation include the Building Effect Parameterization (BEP, (Martilli et al., 2002)), a multi-layer urban canopy model evaluated in Lian et al. (2021). To simulate turbulent motions in the Planetary Boundary Layer (PBL), we use the Mellor-Yamada-Janjic (MYJ) scheme (Janjic, 1990, 1994). This configuration is used for the simulations from December 1st 2019 to April 30th 2020. The ERA5 ECMWF re-analysis fields at 0,75°x0,75° horizontal resolution are used to impose the meteorological initial and boundary conditions. The CO_2 boundary conditions are interpolated from the Copernicus Atmosphere Monitoring System (CAMS; (Inness et al., 2019)) analysis. The biogenic CO_2 fluxes are calculated online in WRF-Chem by the diagnostic biosphere Vegetation Photosynthesis and Respiration Model (VPRM; (Ahmadov et al., 2007, 2009; Mahadevan et al., 2008).

A combination of the high-resolution inventory produced by Origins.earth over IdF and of the global Open-source Data Inventory for Anthropogenic CO_2 (ODIAC) (Oda et al., 2019) is used to simulate fossil fuel emissions over the entire simulation domain. Fig. 1 shows the spatial extent of the high-resolution inventory, which covers most of the metropolitan area.

The Origins.earth inventory provides direct (Scope 1) hourly gridded CO_2 emissions over Paris for six activity sectors (transportation, residential, tertiary, industry including cement, energy, and waste) at the hourly time scale and at 1 km spatial resolution as described in Lian et al. (2022, 2023). The IdF total fossil fuel emissions are scaled to the reported emissions from the french official climate agency (CITEPA). The Origins.earth inventory has been coupled to WRF-Chem and evaluated against CO_2 concentration data from six ground-based stations across the Paris metropolitan region (Lian et al., 2021). The data have been recorded using CO_2 high-precision Picarro CRDS analyzers with WMO/NOAA international calibration standards. This study confirms that our idealized simulations can reproduce the observed CO_2 concentration gradients over the Paris area.

ODIAC is a global gridded inventory of fossil fuel emissions at 1km × 1km spatial resolution and one-month temporal resolution based on power plant profiles and space-borne observations of nighttime lights (Oda et al., 2018). Temporal downscaling was applied to ODIAC using daily and hourly coefficients from the TIMES product of Nassar et al. (2013) to introduce high-frequency variations in the fossil fuel emissions at an hourly scale.

We analyze separately the Paris core urban area (delimited by the light blue line in Fig. 1) to evaluate the potential to retrieve its emissions. The definition of the core urban area can be found in the Supporting Information of Lian et al. (2022). The XCO_2 (and thus XCO_2) enhancements from the core urban area correspond to the plume targeted by the emission estimation methods. Background CO_2 correspond to the remaining contributors to the overall CO_2 fields in the simulation domain, i.e., signals originating from the emissions within D03 but outside the core urban area, from the biogenic fluxes within D03, and from the lateral boundary conditions.

The WRF-Chem simulations provide the "true" CO_2 and meteorological fields. The true signals from the individual flux components

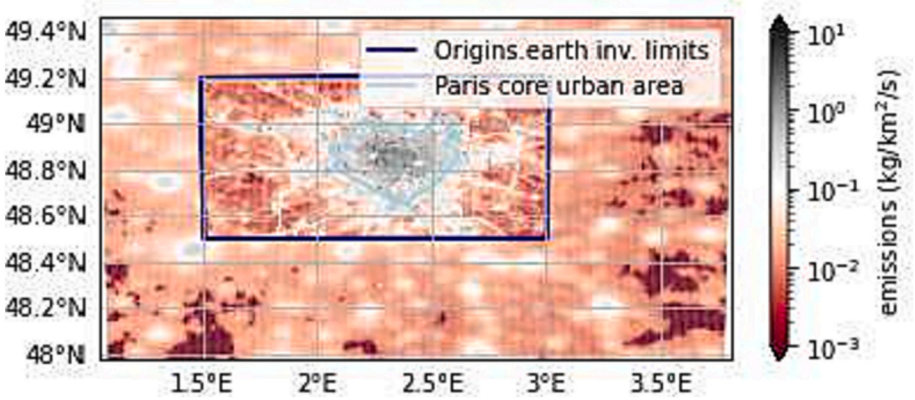

Fig. 1. Illustration of the modelling domain and of the different anthropogenic emission areas whose individual atmospheric signals are traced with WRF-Chem; the Figure shows the anthropogenic emissions on 9/12/2019 at 13:00. Simulations are performed at 1km × 1km resolution. The dark blue rectangle delimits the ODIAC (outside) and Origins.earth (inside) inventories used to prescribe the anthropogenic emissions. The light blue line shows the limits of the Paris core urban area. (For interpretation of the references to colour in this figure legend, the reader is referred to the web version of this article.)

detailed above are traced separately by the model. Among the true meteorological fields, wind, pressure and potential temperature are assumed to be known when applying the emission estimation methods. When analyzing real data, these fields are estimated with significant uncertainties. This corresponds to a source of error that has not been taken into account in this study. However, we discuss in Section 5.1 the potential impact of the uncertainties in the wind fields.

The true CO_2, relative humidity and pressure fields are used to compute the true XCO_2 fields. The computation of the XCO_2 value at longitude *lon* and latitude *lat* follows the simplification proposed by Broquet et al. (2018) to overcome the problem of the partial coverage of the vertical column by the WRF-Chem model:

$$XCO_2(lon,lat) = \frac{1}{P^{surf}_{dry}}\left(\int_{P^{surf}_{dry}}^{P^{Top}_{dry}} CO_2\left(lon,lat,P_{dry}\right)dP_{dry} + < CO_2\left(P^{Top}_{dry}\right)>_{d03} * P^{Top}_{dry}\right) \quad (1)$$

where P_{dry} is the dry air pressure, P^{surf}_{dry} the dry air surface pressure, P^{top}_{dry} (≈50hPa) the pressure at the ceiling of the model and CO_2 the CO_2 dry air mole fraction. The second term of the integral assumes that the portion of the vertical columns of the atmosphere above the top of WRF-Chem corresponds to a homogeneous CO_2 concentration of $< CO_2\left(P^{Top}_{dry}\right)>_{d03}$ (the mean CO_2 concentration at the top of the model over domain 3). The underlying assumption is that the variations in the upper-atmosphere are small and occur over large spatial scales. Therefore, they should not significantly impact local signals in satellite images, which are dominated by regional surface fluxes. Following Broquet et al. (2018) and Santaren et al. (2021), we also assume in this equation that the uniform vertical weighting function is a good approximation of the CO_2 column-averaging kernels associated to actual XCO_2 data. Other realistic choices of the vertical weighting function would not significantly impact the analysis and results in this study.

2.3. Satellite pseudo-images

Five different sampling configurations are used to generate the pseudo-images following three types of satellite observation. First, we use the entire WRF-Chem orthonormal grid at 1 km resolution for D03, which ignores the potential data loss due to clouds and represents a more favorable configuration than that of the future CO2M mission. This full sampling entirely exploits the spatial information on XCO_2 from the model simulation in D03 at the observation time. Second, we use column samples corresponding to actual observation coverages from the OCO missions. We select cases with limited data loss due to clouds and quality control, as we do not apply gap-filling techniques to account for such a loss when using direct flux integration techniques (see Sections 4.5 and 5.3). We select two typical tracks over the area from OCO-2 (OCO Science Team et al., 2020a) at approximately 1.4km^2 resolution and two SAMs from OCO-3 (OCO Science Team et al., 2020b) at approximately 3.7km^2 resolution (cf Fig. 2 and Table 1).

All the corresponding pseudo-images are extracted from the true hourly XCO_2 1-km resolution field between 10:00 and 16:00 (see Section 2.1) We add a noise on the XCO_2 pseudo-data to represent measurement errors, using a Gaussian noise without spatial correlation and with 0.7 ppm standard deviation. This value corresponds to the targeted precision for the individual XCO_2 soundings of the CO2M mission (Sierk et al., 2021), similar to the current precision of OCO-2 XCO_2 measurements (Worden et al., 2017). We choose not to study the effect of error spatial correlations on the inversion skills since the characterization of these correlations has not been documented (Santaren et al., 2020). However, we discuss their potential impact in Section 5.3.

3. Emission estimation methods

The different inversion methods we test here, i.e., the IME, CS and SP methods, and the three versions of the GP inversions (GP1, GP2 and GP3), share sequences of all or some of the following pre-processing steps (Fig. 3): (i) the definition of the plume area (Section 3.6), (ii) the identification of the background field and the separation of the plume signal from the background (Section 3.3), (iii) the identification of the plume centerline (Section 3.4), (iv) the estimation of the effective wind speed and direction (Section 3.6) and (v) the estimation of the area of the urban emissions which corresponds to the detected plume, i.e., the "footprint" of this detected plume (Section 3.8) before (vi) the actual inversion, i.e., the derivation of the fossil fuel CO_2 emissions of the core urban area of Paris based on these different parameters (Section 3.7). We test different techniques for a given step, trying to identify those that are

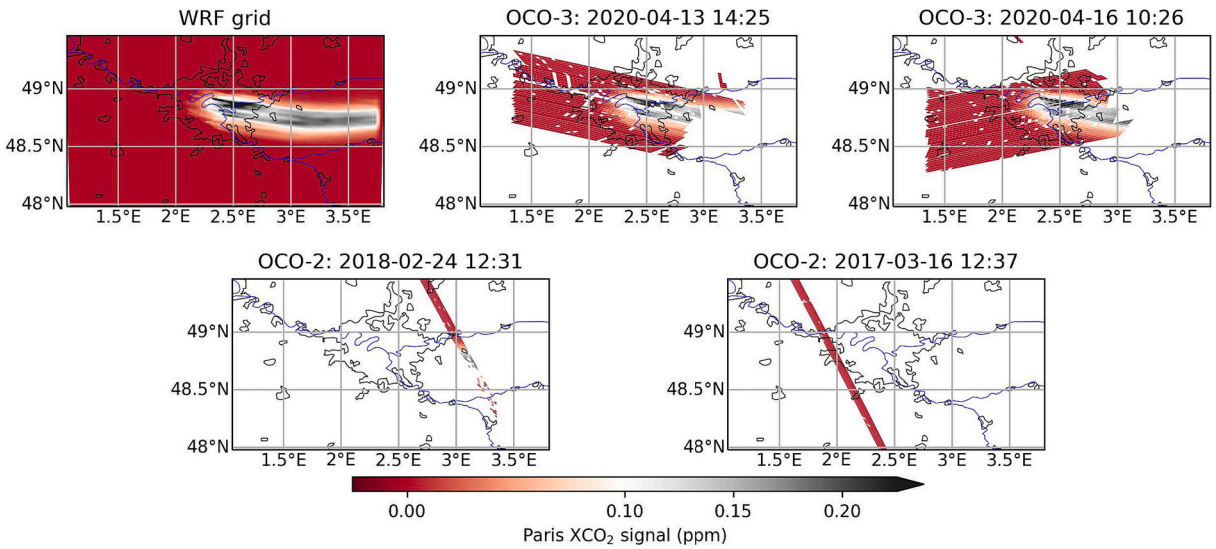

Fig. 2. Illustration of the different sampling configurations used to generate the pseudo-images: application to the WRF-Chem simulation of the XCO_2 anthropogenic signal of the Paris core urban area for 09/12/2019 at 13:00. The titles of the subfigures for the OCO-2 and OCO-3 samplings indicate the corresponding time of acquisition.

Table 1
Main characteristics of the different samplings used to generated the XCO_2 pseudo-images.

	Resolution	Num. of obs. pixels	Dist. to city	Mission	Date
$1km^2$ ref. sampling	$1km^2$	165×200 px	above	None	–
oco2_180224	$\approx 1.5km^2$	533 px	46 km	OCO-2	24/02/2018 12:31
oco2_170316	$\approx 1.3km^2$	897 px	25 km	OCO-2	16/03/2017 12:37
oco3_200413	$\approx 3.6km^2$	2063 px	above	OCO-3	13/04/2020 14:25
oco3_200416	$\approx 3.7km^2$	2003 px	above	OCO-3	16/04/2016 10:26

the most accurate or that provide the most suitable inputs for the inversion. The following sections provide some general insights into these techniques and into the different parameters used for their application. Appendix A.1.1 gives more detailed information on their implementation.

3.1. Definition of the plume area

The true plume area is defined as the set of observation pixels where the true XCO_2 signal from the core urban area is superior to 10^{-6} ppm. This threshold has been set empirically considering the shape and typical amplitude (0.1ppm on average above the city) of the signal from the core urban area in the WRF-Chem simulations. We test two types of methods to identify the plume area when processing the satellite images.

The first type of plume definition methods are denoted *test-based methods* and are adapted from the technique used by Kuhlmann et al. (2019) and Varon et al. (2018). They rely on statistical z-tests to identify observation pixels for which the relatively high XCO_2 values are probably associated with the plume. Our specific implementation of these methods follows five sub-steps (see the Appendix A.1.1). The first step consists in a preliminary estimate and removal of the background concentration on the image. Here, we test 4 options to compute the background concentration. They differ in terms of area of analysis, or in terms of computation of the background in this area. They are denoted: 'bckgp_mean', 'bckgp_med', 'bckgp_2df' and 'bckgp_upw', because they are respectively based on the average, median value, planar fit of the whole XCO_2 image and on the average of the XCO_2 values upwind to the city. The second step consists in a smoothing of the residual image (once

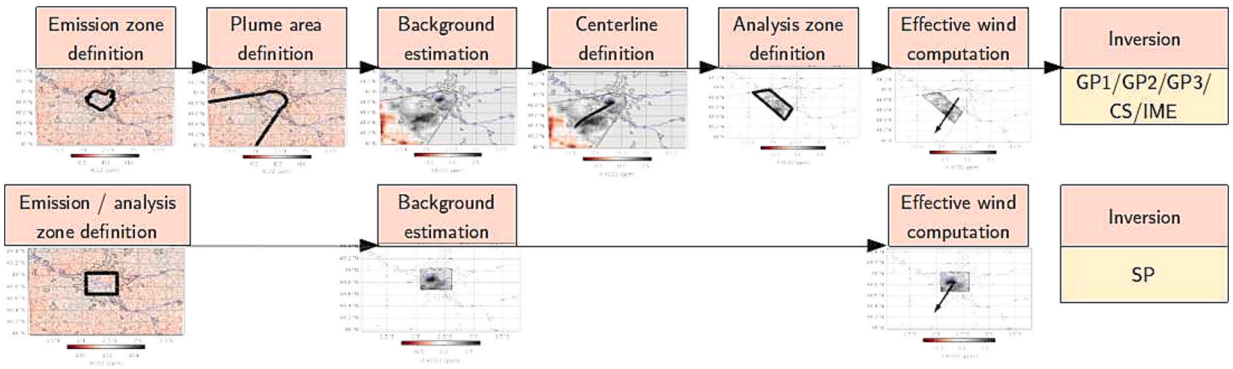

Fig. 3. Summary of the pre-processing steps needed for the different inversion methods. Depending of the method used for the plume definition, the emission zone definition and plume definition can be switch.

the preliminary background estimate has been removed). For each pixel, a new XCO_2 value is defined via a smoothing over its neighborhood area. We test three different types of smoothing with uniform, wiener and gaussian functions, with three different smoothing scales: 10, 20 and 30 km. These smoothing distances are chosen to be of the same order of magnitude as the city radius and, thus, of the plume width in the across-wind direction. These distances provide a good trade-off between the need for large smoothing windows (of several hundred points) and the need to avoid diluting the signal too much. The third step consists in labeling the pixels of the smoothed image when the statistical z-test indicates that the pixels bear a local enhancement likely due to that of the true XCO_2 field rather than to the observation noise. In practice, we label the pixels for which the average value of the surrounding pixels differs from 0 with a confidence of >99% using a 0.7 ppm standard deviation. Finally, the fourth and firth steps consist respectively in a clustering of the labeled pixels with a selection of the cluster corresponding the best to the plume from Paris and in a restriction of this cluster to its portion downwind to the city.

The second type of plume definition method only relies on the direction of the mean wind in the PBL above the core urban area and is denoted wind-based method. The plume area is defined as the area comprised within $\pm 22.5^\circ$ from the direction of the mean wind downwind to the city core urban area. This angle is quite arbitrarily fixed as a compromise, selecting a value sufficiently large to entirely cover curved plumes and sufficiently low to support a suitable derivation of the background (see Section 3.3). The errors from the different preprocessing steps result in errors in the emission estimates during the final inversion. The error in the emission estimates due to errors in the plume definition is evaluated under three different conditions: (i) when knowing perfectly the background field (in which case there is no need to derive a preliminary estimate for this field) (ii) in the absence of noise in the image and (iii) in "realistic" conditions for which we need a preliminary estimate of the background and where noise covers the image. The idealistic conditions of (i) and (ii) allow us to evaluate separately the impacts of the noise and of the background on the plume definition. The experiments in conditions (iii) provide an estimate of their combination.

3.2. Analysis zone

The direct flux integration techniques, the methods based on the Gaussian plume model, and the corresponding computation of the effective wind are applied to a subpart of the plume area. This subpart of the plume area is called *analysis zone*. On the one hand, in areas close to the city, much of the XCO_2 emitted at or near the ground by the city remains near the ground because the vertical mixing in the PBL is not instantaneous. Therefore, the estimation of the effective wind in analysis zones close to the city is challenging. On the other hand, the parts of the plume far from the city correspond to emissions that occurred hours before the acquisition of the satellite image. The inversion methods used here assume that the rate of emissions from the city and the wind are constant. However, the actual emissions and wind fields can vary significantly in time. This is the case in the WRF-Chem simulations that are used to simulate the true XCO_2 fields here (see Section 2.2). Therefore, inversions relying on analysis zones that are far from the city may bear significant uncertainties due to the temporal variations of the emissions and wind over several hours.

We test different types of analysis zone to assess these potential sources of problems and their impact on the different types of estimation techniques: (i) the whole plume area (denoted 'city-∞') (ii) the restriction of the plume area to distances larger than 20 km downwind to the city center ('20 km-∞') (iii) the restriction of the plume area to distances shorter than 40 km ('city-40 km') or 60 km ('city-60 km') downwind to the city center (iv) the restriction of the plume area to distances comprised between 20 km and 40 km ('20 km–40 km') or 60 km ('20 km–60 km') downwind to the city center. Note that the SP method does not rely on a definition of the plume area: the analysis zone for this method is defined as the square of length $L_{SP} = 40$km centered on the city center, and is called the "source area".

3.3. Background estimation

Six methods (m_i) are tested for the main estimation of the background values ($XCO2_{m_i}$), which are used to derive the XCO_2 signal associated to the plume. Some of them cannot be applied when using SP for the final inversion. The methods denoted 'bckgl_mean', 'bckgl_med' and 'bckgl_2df' derive the mean, median or planar fit of the XCO_2 value at the "edges" of the source area when using the SP inversion method (see Section 3.2), or of the plume area when using the other inversion methods. Edges are defined as pixels located within 8 km from the limits of the source or plume area. The value 8 km has been chosen empirically. The method denoted 'bckgl_upw' derives the mean XCO_2 value upwind to the plume area. 'bckgl_bih' and 'bckgl_gau' extrapolate the XCO_2 field from the whole image to the source or plume area using biharmonic functions, or Gaussian kernels giving more weight to the vicinity of the plume area. Finally, 'bckgl_cs' partitions the plume area and its edges into narrow sections normal to the plume direction (see Section 3.5) and computes a linear background for each of these cross-sections. More details about the methods can be found in Appendix A.2.

Uncertainties in the emissions estimates due to errors in the background estimation are quantified under three different conditions: (i) in the absence of noise in the image and with a perfectly-known plume area, (ii) with a perfectly-known plume area but with noise, and (iii) in "normal" conditions for which the plume area must be detected within a noisy image. Our results under perfect conditions allow us to discard from the outset of the analysis some of the proposed approaches showing poor performances.

3.4. Plume centerline

We can define the plume centerline as the curve following the effective vertically-averaged wind driving the XCO_2 plume from the city center. Since the actual wind direction varies in space and time, this centerline is often not straight. It is identified in the $\delta XCO2_{sm,N}$ field obtained by removing from the XCO_2 image the background estimate $XCO2_{m_i}$ and by smoothing the resulting field to filter the noise following the same smoothing method as that described in Section 3.1. We test two methods to identify the plume centerline in this field. Both derive the centerline as the curve that best fits the ensemble of pixel locations within the plume area, each pixel location being weighted by its $\delta XCO2_{sm,N}$ concentration (similarly to Kuhlmann et al. (2020)). The first approach uses a linear fit, while the second uses a fifth-order polynomial fit. As expected, the linear fit shows poor performance when the plume is strongly curved. However, when the plume is straight, the polynomial fit overfits residual observation noise and background in the smoothed $\delta XCO2_{sm,N}$ field.

We do not attempt to derive the actual plume centerline based on the full knowledge of the true meteorological and CO_2 fields. This limits our ability to quantify the uncertainties associated with the definition of the plume centerline. However, uncertainties due to the centerline mislocation are part of the total uncertainties in the derivation of the emissions that are diagnosed in our experiments.

3.5. Plume cross-sections

The GP3 and CS inversion methods, one of the effective wind computation method ("tangent wind" method, see Section 3.6) and the 'bckgl_cs' background estimation method rely on the partition of the plume area into cross-sections. Those cross-sections consist of bands that are normal to the plume centerline. In practice, we sample points along the plume centerline with a constant arc length of 5 km. We then derive

the normal to the plume centerline on each of these points. Those normal lines delimit the plume cross-sections. Therefore, a cross-section has a 5 km width. Other widths have been tested, but the sensitivity to this parameter was low (see Appendix B.1.2).

For each cross-section, we define the node as the center of the corresponding portion of the centerline. When GP3 is used for the final inversion each cross-section (i_{cs}) is further partitioned along the normal to the plume centerline in small portions of 5 km length (i.e. these portions have a 5 km × 5 km size). The coordinates of each portion of each cross-section are defined as (i) the curvilinear abscissa of the cross-section node (denoted s) and (ii) the distance along the corresponding cross-section between the cross-section node and the portion center (denoted n). This coordinates system, which forms a non-regular grid (Fig. 4), is used to define the complex Gaussian plume model that is used in the GP3 method.

3.6. Effective wind computation

The effective wind is defined as the vertically-integrated wind driving the XCO_2 plume. The vertical integration of the "true" effective wind is thus weighted by the vertical distribution of the CO_2 mass (see Section A.3). When the vertical distribution of CO_2 is unknown, effective wind estimates rely on simple assumptions regarding this distribution. We test three methods of vertical integration or sampling of the 3D wind field, this field being perfectly known for the emission estimates in our experiments (see Section 2.2).

The first method computes the mean wind in the PBL, assuming that the plume can rapidly mix within the PBL, downwind to the city. The second method uses the 10-m surface wind with a multiplicative coefficient, as proposed in Varon et al. (2018). The multiplicative coefficient representing the relationship between the 10-m surface wind and the plume effective wind is derived from meteorological simulations, here in the analysis zone '20 km–40 km'. The third method (denoted tangent wind hereafter) uses the wind sampled at the vertical level for which the plume direction aligns the most with the wind direction (i.e., the wind direction that aligns most with the tangent of the centerline). More details can be found in Appendix A.3.

These methods are used to derive estimates of the 2D field of effective wind $W_{eff}(x,y)$. These 2D estimates $W_{eff}(x,y)$ are then averaged horizontally over the cross-sections, the source area and the analysis zone respectively for the CS method, the SP method and for the other inversion methods to derive a single value of the horizontally average effective wind W_{eff}^{av}. This horizontal average weights the values of $W_{eff}(x,y)$ by the corresponding values of $\delta XCO2_{sm,N}$. These different methods to compute the effective wind depend more or less on the previous pre-processing steps. The horizontal weighted average of the effective wind depends on the plume area and background computation. The definition of the plume centerline (and thus the computation of the plume area and the background) is a critical step in the computation of the effective wind per cross-section in the tangent wind method. The methods are evaluated under three different conditions: (i) with perfect knowledge of the XCO_2 signal from the Paris core urban area; (ii) with a perfectly-known plume area and background and with noise in the image; and (iii) under "normal" conditions (with unknown plume and background, and with noise).

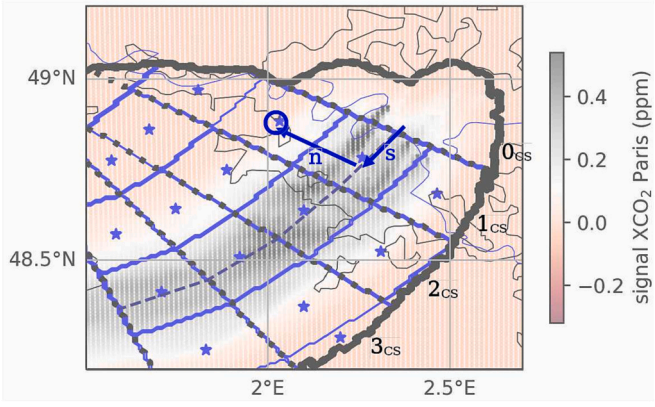

Fig. 4. Illustration of the cross-sections definition: example with the application to the true XCO_2 field from the Paris core urban area on December 1st 2019 at 10:00 and with the definition of the plume centerline based on a 5th order polynomial fit. In this figure the width of the cross sections is set to 20 km instead of 5 km for the sake of visibility. The blue dashed line indicates the centerline of the plume, the plain black line indicate the plume, the dashed black lines delineate the cross-sections, the blue lines delineate the portions used to build the complex Gaussian plume model (with a 20 km × 20km instead of 5 km × 5km size for better visibility) and the blue stars indicate the centers of these portions. (For interpretation of the references to colour in this figure legend, the reader is referred to the web version of this article.)

3.7. Inversion methods

The details on our implementation of the IME, CS and SP methods and of the GP inversions are given in A.4. The IME method (whose version used here is slightly modified from Frankenberg et al. (2016); Varon et al. (2020)) computes the total mass present in the analysis zone and divides it by the estimate of the time of residence of the CO_2 molecules in this zone. The SP method, adapted from studies which focused on point sources such as Buchwitz et al. (2017) and Varon et al. (2018), computes the total mass in the source area (see Section 3.2) and divides it by the estimate of the residence time of CO_2 molecules in this area. The CS method (Krings et al., 2011; Kuhlmann et al., 2020; Varon et al., 2019) first computes the flux of CO_2 across each of the plume cross-sections within the analysis zone (see Section 3.5): this results in one emissions estimate per cross-section. The final emissions estimate of the CS method is the median of the estimates from the different cross-sections. However, in the first part of Section 4.1, we will investigate the different emissions estimates from the individual cross-sections to optimize some of the parameters of the pre-processing steps, such as the method used to define the plume centerline and the definition of the analysis zone within the plume area.

The GP inversions use the general formulation of the Gaussian plume model for extended sources used by Krings et al. (2011). The inversions consist in fitting the Gaussian plume models to the total column mass enhancement associated with the plume from the city derived from the XCO_2 images by optimizing in the model some of the following parameters: the emission from the emission zone, the radius of this emission zone, the direction of the effective wind and the Pasquill stability parameter of the atmosphere. Three variants of the Gaussian model or the inversion parameters are tested. In the first variant, denoted "simple Gaussian plume model inversion" (GP1), the radius of the emission zone, the Pasquill parameter and the direction of the effective wind are fixed (see Appendix A.4 for values). In particular, the radius of the emission zone is fixed so that it corresponds to the Paris core urban area. The optimization thus only applies to the emissions from the Paris core urban area. In the second variant, denoted "intermediate Gaussian plume inversion" (GP2), the emission and the radius of the emission zone, the direction of the effective wind and the Pasquill stability parameter are optimized simultaneously. In the last variant, denoted "complex Gaussian plume inversion" (GP3), the model is adapted to turning plumes by applying the Gaussian plume formulation to the non-regular grid defined in Section 3.5. In that case, the wind direction is fixed by construction, while the emission and the radius of the emission zone, and the Pasquill stability parameter are optimized together.

The inversion methods are first evaluated under idealized conditions in the absence of noise in the image and for which the XCO_2 signal from the Paris core urban area (i.e., the plume area and the background) and the effective wind are perfectly known. These first tests are used to select

the most suitable methods for defining the plume centerline and cross-sections. Most of the tests of the methods with more realistic conditions correspond to the extension (with the propagation of error up to the emission estimates) of the tests used to evaluate the different pre-processing steps detailed above.

3.8. Definition of the emission zone corresponding to the emission estimates

The analysis zone can correspond to a fraction of the city core or, on the opposite, to a broader area. A precise definition of this footprint, called "emission zone" hereafter, can be used to rescale the emission estimates to better correspond to the core urban area.

The SP method requires a pre-determined emission zone: the "source area". For the other methods the definition of the emission zone depends on the method used to define the plume area. For the CS method, we associate an emission zone to each cross-section.

When using the wind-based method for the definition of the plume area, the definition of the emission zone is assumed to be, by construction, the core urban area itself. There is an exception when a cross-section of the CS method overlaps a portion of the core urban area. In such a case, the emission zone is defined as the fraction of the core urban area upwind to the cross section (following the effective wind estimate).

When using test-based methods to define the plume area, the definition of the emission zones differs between the CS, GP and IME methods (see Fig. 5). For the cross-sections of the CS method downwind to the core urban area and for the IME method, the emission zone combines all the emissions upwind to the cross-section and analysis zone (respectively) from or close to the core urban area. For the cross-sections of the CS method overlapping with the core urban area, the emission zone is the fraction of the core urban area upwind to these cross-sections. For GP inversions, we define the emission zone as the circle centered on the city center. The radius of this circle is the "radius" parameter of the Gaussian plume model fixed or optimized by the inversion (cf. Section 3.7).

Finally, we compute the ratios in the true emission maps between the total emissions of the Paris core urban area and the emissions within the emission zones. These ratios are used to rescale the estimated emissions to have an emission estimation for the Paris core urban area. Here, we assume that this rescaling can rely on a perfect knowledge of the ratios. However, in real inversions conditions, there are uncertainties in the spatial distribution of the urban inventories, and thus, the derivation of these ratios is a source of uncertainty when dealing with actual observations, which is ignored here. Future studies should also account for this ratio uncertainty. When using the CS method, emissions estimates per cross-section are rescaled using the corresponding emission zone for each cross-section. The final estimate of the CS method is based on the median of this rescaled ensemble.

In order to evaluate the need for such a definition of the emission zone, we will compare the errors in the emission estimates for the Paris core urban area when using the crude emission calculation or when rescaling it according to the emission zone.

3.9. The different error components: Summary of the different sets of tests

Fig. 6 summarizes the different tests to compute the errors associated with the pre-processing and inversion steps and defines the notation for these errors. We start from an ideal case with a perfect knowledge of the true background, effective wind an plume area and without measurement noise. The corresponding errors in the estimates of emissions from the Paris core urban area at the overpass time are denoted ε^0. Then, we introduce the sources of errors step by step. When all sources of error are accounted for, we get the total errors in the emission estimates denoted $\varepsilon^{\text{comb}}$. In between, the statistics of the additional error in the emission estimate $\varepsilon^{\text{new}}_{\text{previous}}$ due to the incremental sources of errors is studied at each step by computing the difference between the emission estimate from the new step and that from the previous step in the tree, normalized with the division by the true emission of the Paris core urban area at the overpass time. For ε^0 and $\varepsilon^{\text{comb}}$, the difference is made with the true emission of the Paris core urban area at the overpass time.

The notation for the errors $\varepsilon^{\text{new}}_{\text{previous}}$ is as follows: the "new" letter in superscript indicates the corresponding source of error while the "previous" letters in index indicate the sources of errors on the top of which it is added and estimated. Therefore, the tests used to compute these errors combine the sources of errors labeled in index and superscript. The "w", "b" and "p" letters indicate the uncertainties respectively in the effective wind, background and plume area, and the "n" indicates the observational noise. For example, ε^p_b (top box in Fig. 6) is the difference between (i) the emission estimate when there are uncertainties in the background and plume area, and (ii) the emission estimate when there are uncertainties in the background only, divided by the (iii) true emissions.

We characterize the distribution of these errors, which can deviate from a gaussian distribution, with their median and interquartile range (denoted IQR). We also provide the 15.9% and 84.1% quantiles, as they would represent the ± 1-standard deviation interval if the distributions were gaussians.

3.10. Temporal representativity of the plume

City plumes are driven by emissions and winds that can vary

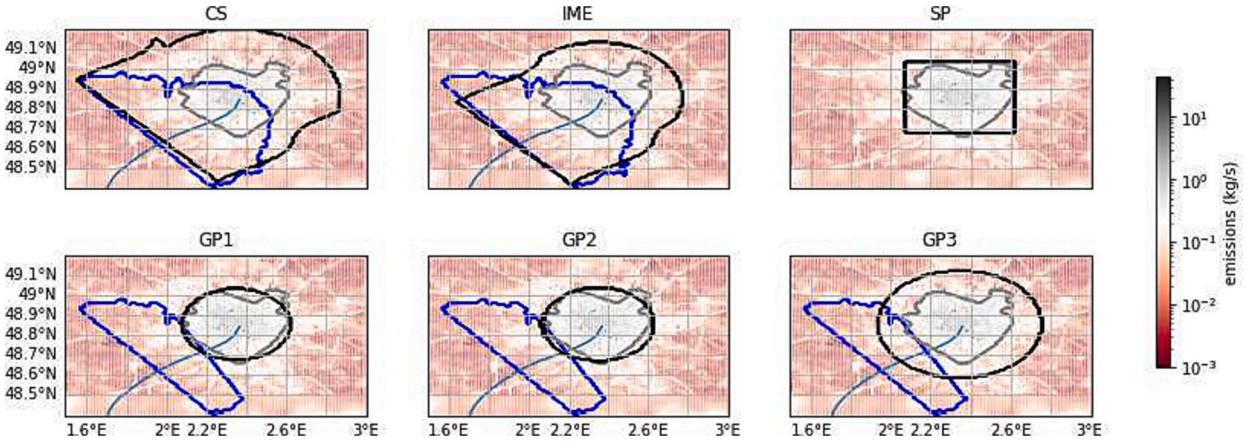

Fig. 5. Illustration of the analysis zone and emission zone when using the wind-based method for the definition of the plume area on 1/12/2019 at 10 a.m. The blue line indicates the analysis zone, the gray one the Paris core urban area and the black one the emission zone for the different inversion methods. The analysis zone used are 'city-40 km' for CS and IME, and '20 km–40 km' for the gaussian plume inversions. (For interpretation of the references to colour in this figure legend, the reader is referred to the web version of this article.)

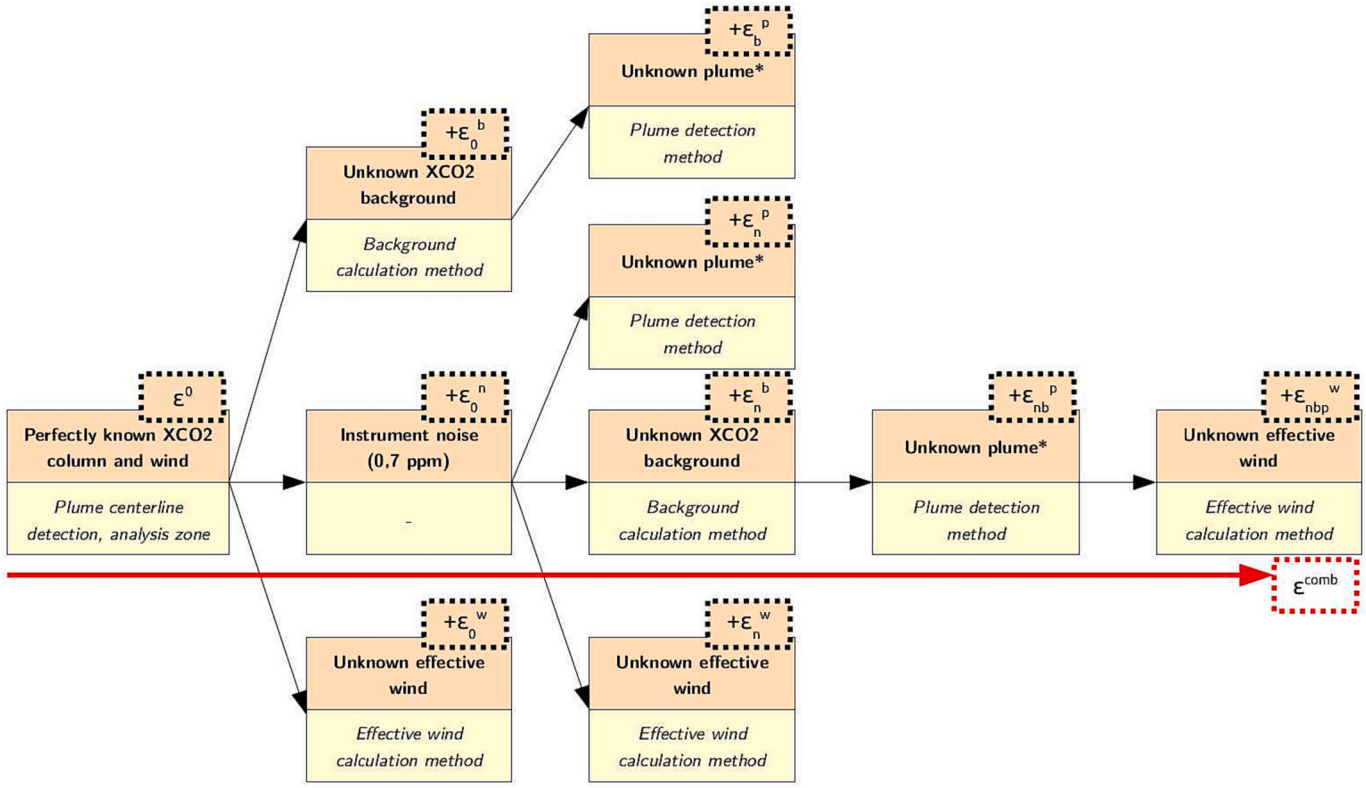

Fig. 6. Summary of the different error components. * indicates that the step is not applied to the SP method (which does not need a detection of the plume area).

significantly over a few hours. However, we evaluate our emissions estimates by comparing them to the true emissions at the satellite observation time. Similarly, the effective wind is based on the wind field at the satellite observation time. In the CS method, temporal variations in the emissions can be considered in the emissions calculation. Indeed, for each cross-section, we can derive a time corresponding to the emission estimate (equal to the distance between the cross-section node and the city center divided by the mean effective wind speed). Section 4.1 will analyze the fit between these estimates from individual cross-sections and the actual emission from the core urban area at the corresponding time.

However, in practice, from Section 4.2, the selection of parameters for the plume analysis zone will discard any data located further than 60 km away from the city center. As detailed in Section 4.1, we will also indirectly filter out days with low wind speed by discarding days when the spatial variability of the wind direction is high. Therefore, 92% of the data that will be used for the final analysis will correspond to CO_2 emitted within the previous 2 h. Within such a short time frame, temporal variations remain limited and will znot be considered in our uncertainty analysis.

4. Results

4.1. First comparison of the inversion methods and selection of their configurations

Here we study ε^0 and its dependency on the meteorological conditions and on the parameters of the inversion methods to narrow the range of appropriate options and parameters for the configuration of these methods. The tests are performed with a perfectly-known plume,

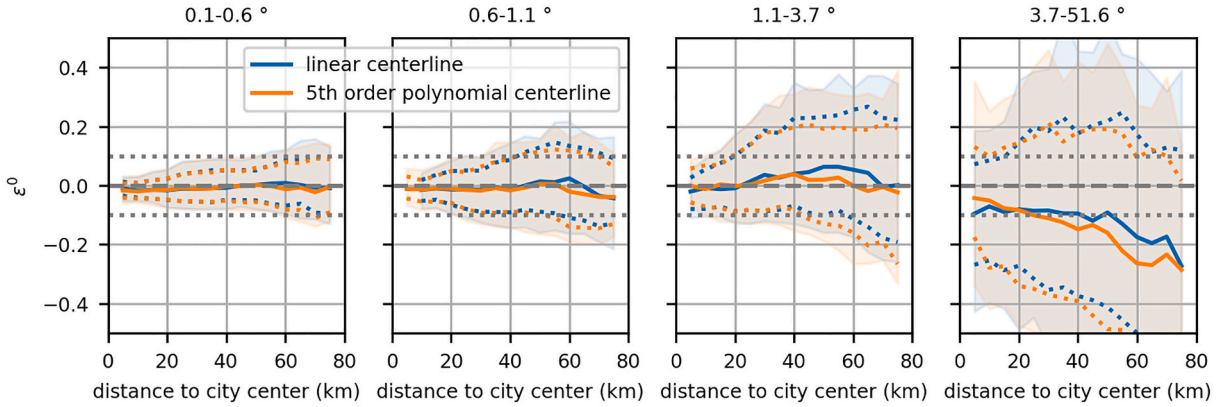

Fig. 7. Distribution (median in plain line, 1st and 3rd quartiles in dotted line, 15.9–84.1% quantiles range shaded) of the error ε^0 for estimates of the emissions per cross-section as a function of the distance between the cross-section and the city center when applying the CS method. Each figure shows a binning of the result for a quartile of the standard deviation of the spatial variability of the wind direction. Results are obtained with a linear (blue) or fifth order polynomial (orange) fit for the centerline. (For interpretation of the references to colour in this figure legend, the reader is referred to the web version of this article.)

background, and effective wind. In general, all inversion methods give accurate results (with low bias and low IQR of ε^0) when the meteorological conditions favor the ventilation of the emitted CO_2 in a weakly spread and straight plume. These conditions are characterized by high wind speed and low wind direction variability (see an illustration in Fig. 7). However, when the emitted CO_2 accumulates over Paris into a large plume with high XCO_2 values or forms a plume with a complex structure, the results bear significant errors. Those situations can be driven by low effective wind speeds or large variations in wind direction in space (horizontally and vertically) and time (over the few hours before the observation time). We characterize the spatial variability of the wind direction via the circular variance of the 3D wind field in the PBL at the observation time. It has a correlation of −0.8 with the mean wind speed in the PBL. Therefore, this spatial variability appears to be a good index of the main meteorological conditions that challenge the inversion methods.

Fig. 7 illustrates the general increase of ε^0 when this spatial variability increases with the example of results from the CS method (see Appendix B.1.2 for the similar results from the other methods). It also illustrates the error sensitivity to the distance between the analysis zone and the city center. More specifically, it shows that when applying the CS method to individual cross-sections, the IQR of ε^0 increases with the distance between the cross-sections and the city center for any level of spatial variability in the wind direction. The CS method shows a loss of precision over remote parts of the plume, which correspond to a longer period of transport and, thus, to larger levels of atmospheric diffusion and larger temporal variability in the wind during the corresponding period. Indeed, the diffusion increases the overlapping between the signal from different hours of emission (Broquet et al., 2018). The temporal variability of the wind during the travel time from the city to the cross-section (or, more generally, to the full extent of an analysis zone, see Appendix B.1.2) challenges the stationarity assumption underlying the different inversion methods. However, the bias increase at distances higher than 60–70 km away from the city is fed by an artifact: at this typical distance from the city, some of the cross-sections are cropped by the image borders (depending on the plume direction).

The study of the sensitivity of the distribution ε^0 to the options for the inversions focuses, in the following, on the sensitivity to the centerline computation methods and to the definition of the analysis zones for the CS, IME and GPs methods. We also use a first comparison between the results from the different GP methods to assess the relevance of using the three of them. Since we have a single configuration for the SP method, this method is ignored in these first tests of sensitivity.

The sensitivity of the distribution ε^0 to the options for the centerline definition is low, even when tested on the GP3 inversion. The bias is just slightly lower when using a centerline based on a fifth-order polynomial fit when the spatial variability of the wind direction is moderate to high, as illustrated in Fig. 7 with the CS method.

As explained above, the IQR of the distribution of ε^0 increases with the distance of the analysis zone to the city center. However, the sensitivity of the bias of the distribution of ε^0 to the analysis zone differs depending on the type of plume inversion method: CS and IME following a mass-balance approach or Gaussian plume inversions. The mass loss at the image borders (where the plumes are cropped) causes a slight underestimation (1–2%) of the emissions with the IME and CS methods when the analysis zone covers the fraction of the plume beyond 60 km (i.e., with the 'city-∞' and '20 km-∞' analysis zones). The Gaussian plume model inversions rely on the fit to the individual XCO_2 concentrations per available observation pixel rather than on a mass balance. Therefore they are not biased by the plume cropping at the image borders. However, due to the approximate modelling of the emission spatial distribution in the Gaussian models used here, the GP inversion underestimate the spread of emission source along the wind direction. Therefore the emissions are underestimated by the GP inversions when the analysis zone overlaps the Paris core urban area (i.e., with the 'city-40 km', 'city-60 km' and 'city-∞' analysis zones), with 6 to 12% biases for the intermediate and complex Gaussian plume inversions.

The simplest Gaussian plume inversion method yields substantial (16 to 19% in absolute values) biases, which can be attributed to the lack of flexibility to fit complex shape of the actual plumes. The stability parameter and the radius of the emission zone, both pre-determined in this method, are generally far from those derived by the other Gaussian plume inversion methods. For example, in GP1, the radius of the emission zone if fixed to that of the Paris core urban area, i.e., to 20 km. However, in GP2 and GP3, the distributions of the retrieved radius of the emission zone have a median ranging from 27 to 29 km, depending on the analysis zone (cf Appendix B.1.2).

Following these first insights, we narrow the options for the inversion methods. Only the fifth-order polynomial fit is kept for the centerline definition. The analysis zones 'city-∞' and '20 km-∞' are not kept for any of the plume inversion methods and only the '20 km–40 km' and '20 km–60 km' analysis zones are retained for the GP inversion methods. The GP1 method is left out. For the following analysis, we also discard the cases for which the spatial variability of the wind direction is superior to 7° (17% of the images). This selection discards most of the days with low wind speed due to the correlation between the wind speed and the spatial variability of the wind direction. It reduces the IQR of the distribution of ε^0 from 11%–17% to 9%–15%.

4.2. Narrowing the range of options for the pre-processing steps

The analysis in this section are used to select most suitable methods to address the pre-processing steps. The final analyses presented in sections 4.4 and 4.5 will rely on this selection of the methods.

4.2.1. Evaluation of the wind calculation methods

We assess the wind calculation methods based on the analysis of the distributions of ε_0^w and ε_n^w. Both distributions show a low bias (<5% in absolute value) but a high IQR (between 29% and 38%, cf. Table 2 and Appendix B.2.1 and B.2.2) when using the tangent wind method. Conversely, when using the mean and surface wind methods, the IQR of the errors is small (between 10% and 30%), but the bias is significant (up to 43% in absolute value). Biases in both ε_0^w and ε_n^w distributions decrease with the distance of the analysis zone to the city center when using the mean wind method. In particular, they are low when using the '20 km–40 km' and '20 km–60 km' analysis zone, i.e., analysis zone at >20 km from the city center, since the corresponding part of the CO_2 plume is well mixed in the PBL. Overall, the mean wind method produces errors with biases slightly larger than those obtained with the tangent wind method (between 7% and 11%) but with a much smaller IQR (<14%) for the '20 km–40 km' and '20 km–60 km' analysis zones. Therefore, we select the method of wind estimation as a function of the analysis zone. The tangent wind is used with the 'city-40 km' and 'city-60 km' analysis zones, while the mean wind in the PBL is used with the '20 km–40 km' and '20 km–60 km' analysis zones. The surface wind method is not retained hereafter for two main reasons: its lower precision (with an IQR of ε_0^w and ε_n^w between 14% and 23%) compared to the mean wind method, and the need for precise information from meteorological model simulations for the derivation of the multiplicative coefficient used to convert 10-m surface wind into effective wind (Varon et al., 2018).

4.2.2. Evaluation of the background calculation methods

The assessment of the background calculation methods is based on the analysis of ε_0^b and ε_n^b but also on the direct comparison between the background concentration estimate and the true values of the background concentrations in the analysis zone. The median of the differences between these background concentrations is studied as the "background error". Even though there is no strict relationship between

Table 2
Range of the median (med.) and interquartile range (IQR) for the different error distributions in function of the methods tested for a given step. Here, ε^{comb} distributions are calculated after the selection of the most suitable methods for the of the plume definition, background calculation and effective wind estimation.

		wind method			bckg. calc. method			plume detect. method			analysis zone			
		tangent wind	mean wind	surface wind	bckgl_xxx	bckgl_cs	bckgl_gau	test-based, wo/ rescaling	test-based, w/ rescaling	wind-based	city-40 km	city-60 km	20 km–40 km	20 km–60 km
ε^{0}		Used for inversion methods parametrization (cf Section 4.1).												
ε_0^w	med.	[−4%;6%]	[8%;37%] ([7%;11%])[1]	[−43%;9%] ([−3%;9%])[1]										
	IQR	[24%;36%]	[8%;21%] ([8%;10%])[1]	[12%;30%] ([13%;16%])[1]										
ε_n^w	med.	[−3%;3%]	[6%;36%] ([6%;11%])[1]	[−32%;9%] ([3%;9%])[1]										
	IQR	[20%;36%]	[8%;25%] ([8%;13%])[1]	[11%;33%] ([14%;20%])[1]										
ε_b^0	med.				cf. Appendix	[−3%;13%]	[−10%;13%]							
	IQR				B.4.1	[57%;70%]	[47%;63%]							
ε_b^n	med.				cf. Appendix	[−1%;12%]	[−3%;11%]							
	IQR				B.4.2	[58%;84%]	[51%;70%]							
ε_n^p		Used for parametrization of thest-based methods for plume definition (cf Appendix B.3).												
ε_b^p	med.					[−3%;15%][2]	[−8%;1%][2]	[−3%;22%][3]	[−27%;1%][3]	[−8%;1%][3]				
	IQR					[38%;76%][2]	[25%;58%][2]	[36%;75%][3]	[34%;58%][3]	[25%;58%][3]				
ε_{nb}^p	med.					[4%;16%][2]	[−8%;6%][2]	[−21%;-6%][3]	[−34%;-16%][3]	[−8%;6%][3]				
	IQR					[42%;90%][2]	[34%;68%][2]	[49%;78%][3]	[42%;70%][3]	[34%;68%][3]				
ε_{nbp}^w		Not used for parameter selection.												
ε^{comb}	med.										[−7%;7%]	[2%;17%]	[8%;13%]	[11%;26%]
	IQR										[72%;74%]	[75%;78%]	[73%;92%]	[78%;100%]

[1] results obtained with the ‘20 km–40 km and ‘20 km–60 km analysis zones.
[2] results obtained with the wind-based method for the plume definition.
[3] results obtained with the bckgl_gau method for the background calculation.

such a definition of the background error and ε_0^b and ε_n^b, results confirm that the distribution of the background error and of ε_0^b and ε_n^b are strongly linked.

For the estimate of the background corresponding to the analysis zone of the IME, CS and GP methods, the local methods, i.e., 'bckgl_gau' and 'bckgl_cs', outperform the other methods. These local methods yield background errors with biases of <0.01 ppm and with IQR ranging between 0.06 ppm and 0.1 ppm, which is lower than the biases or IQR obtained with the other methods, both when processing images without noise and when processing images with noise, and regardless of the option taken for the analysis zone. Indeed those other background calculation methods yield background errors with a high IQR ([0.09 ppm;0.11 ppm], [0.09 ppm;0.17 ppm] and [0.08 ppm;0.12 ppm] for 'bckgl_mean', 'bckgl_upw' and 'bckgl_med' respectively) or a high bias (>0.01 ppm for 'bckgl_bih' and 'bckgl_2df'). Accordingly, the values of ε_0^b obtained with the methods 'bckgl_mean', 'bckgl_upw', 'bckgl_med', 'bckgl_bih' and 'bckgl_2df' are higher than those obtained with the local methods. Therefore, these methods are discarded at this stage of the analysis. Furthermore, the analysis of ε_b^p reveals that when the plume is unknown, the overall errors from the plume definition and background estimation are larger when using the 'bckgl_cs' method than when using the 'bckgl_gau' method (Table 2 and Appendix B.5.2 -Fig. S12-). This supports the selection of the 'bckgl_gau' method only for the background estimation when using the IME, CS and GP methods.

For the background estimation when using the SP method, the 'bckgl_gau' method yields background errors with a smaller bias and IQR (0.00 ppm and 0.08 ppm) than that from the 'bckgl_mean' method (−0.01 ppm and 0.09 ppm). Therefore, 'bckgl_gau' is the most suitable method for all the inversion methods. We select it as the unique background calculation method in the following.

4.2.3. Evaluation of the methods for the definition of the plume area

The assessment of the methods for the definition of the plume area is based on the analysis of ε_n^p, ε_b^p and ε_{nb}^p. We first try to derive the optimal configuration for the test-based methods and the corresponding sub-steps (in particular, the preliminary computation of the background and the smoothing of the image prior to the statistical z-test). Results show that when using these methods (see Appendix B.3 and B.5), the distributions of ε_n^p, ε_b^p and ε_{nb}^p are sensitive to the smoothing scale and to the preliminary background calculation method. However, the choice of the function for the smoothing has a marginal impact on the results: we thus retain the uniform smoothing, which is easier to apply to complex observation sampling. When using small smoothing scales, the parts of the plume with a low signal are missed by the statistical z-test. In contrast, when using large smoothing scales, the statistical z-test tends to retain pixels that do not belong to the actual plume and thus to enlarge artificially this plume. We fix the smoothing scale to 20 km, which leads to the smallest errors. The analysis of ε_b^p and ε_{nb}^p also indicates that the best method for the preliminary background computation is 'bckgp_mean'. Therefore, the only configuration we keep for the test-based method uses 'bckgp_mean' for the preliminary background computation, the 20 km scale uniform smoothing and the standard z-test and clustering presented in Section 3.1.

The rescaling of the emission estimation to account for the difference between the emission zone of the plume definition and the Paris core urban area when using the test-based method (see Section 3.8) reduces the IQR of the distributions ε_b^p (from 45–98% to 42–77%) and ε_{nb}^p (from 61–107% to 53–99%). However, this rescaling introduces a negative bias: the distribution ε_b^p (resp. ε_{nb}^p) has a bias between −27 and − 1% (resp. -38 and −16%), whereas the bias is between −3 and 21% (resp. -28 and −6%) without rescaling. Therefore, we do not retain this rescaling.

The final selection of the plume definition method is based on comparing this configuration of the test-based method and the wind-based method. The test-based and wind-based methods produce similar distributions of ε_n^p. However, the IQR of the distribution of ε_b^p is smaller when using the wind-based method : 30 to 69% using the wind-based method, 45 to 97% errors when using the testbased method. Biases in ε_b^p are smaller when using the wind-based method compared to the test-based method (with values ranging between −7% and + 1% and between −3% and + 22% respectively). When noise is added to the image, the error distribution ε_{nb}^p from the test-based methods shows a non-negligible bias (from −6 to −29%), whereas biases obtained with the wind-based methods remain between 16 and − 10%. Therefore, we select the wind-based method as the unique plume definition method for the following analysis.

4.2.4. Evaluation of the analysis zones

The choice of the analysis zone impacts each step (plume inversion, background and wind calculation, and the definition of the plume area) of the overall emissions estimation with the CS, IME and GP methods. This complicates the assessment of the best option for this choice. For example, the choice of the analysis zones which are the closest to the city results in a smaller IQR for ε^0, but larger for ε^w (see Sup. Mat. B.1.2 and B.2.1). Therefore, our assessment focuses on analyzing the distribution of ε^{comb}. For all inversion methods, the IQR of ε^{comb} increases with the distance of the analysis zone to the city (Table 2). We thus select the 'city-40 km' analysis zone for the CS and IME methods and the '20 km–40 km' analysis zone for the GP inversions.

Fig. 8 summarizes the list of configurations that are selected for the following analysis.

4.3. Filtering the background conditions

The analysis of the results from the list of emission estimation configurations presented in Fig. 8 reveals a strong sensitivity of ε^{comb} to the complexity of the background field (strongly driven by the contribution from the biogenic fluxes), in addition to that of the meteorological conditions (see Section 4.1). In the following, we characterize this complexity by the spatial variability (the standard deviation) of the XCO_2 field over the whole image. The IQR of ε^{comb} scales primarily with the ratio between the mean XCO_2 signal in the plume area and the variability in the XCO_2 field, whereas the bias of ε^{comb} is mainly due to the background error (as defined in Section 4.2). By filtering out images with large variability in XCO_2 signals (> 0.75 ppm) and with a large spatial variability of the wind direction (see Section 4.1), the error ε^{comb} decreases by 13 to 22%, depending on the emission calculation method, while removing 43% of the 1064 initial pseudo-images. More specifically, its IQR decreases from 99% down to 78% with the IME method, from 100 to 89% with CS method, from 109 to 89% with SP method, from 94 to 74% with GP2 inversion and from 103% to 78% with GP3 inversion.

4.4. Error analysis with the selected emission estimation configurations and cases

Fig. 9 shows the distribution of the different error components when filtering out images following the criteria defined in Sections 4.1 and 4.3 on the spatial variability of the wind direction and of XCO_2. The distributions ε^{comb} (the total error) obtained with the different emission estimation methods are similar, with bias inferior to 10% and IQR between 74 and 89%, except when using the SP method that leads to a bias of 38% and an IQR of 89%.

The analysis of the error components (Fig. 9) shows that the background calculation step is the main source of error for all emission estimation methods. Indeed, the IQR of the distributions of ε_0^b and ε_n^b are between 54 and 71%, whereas the IQR of the other error component are below 58%. The second most important error source is the estimation of the effective wind. Indeed the distributions ε_0^w, ε_n^w and ε_{nbp}^w show large

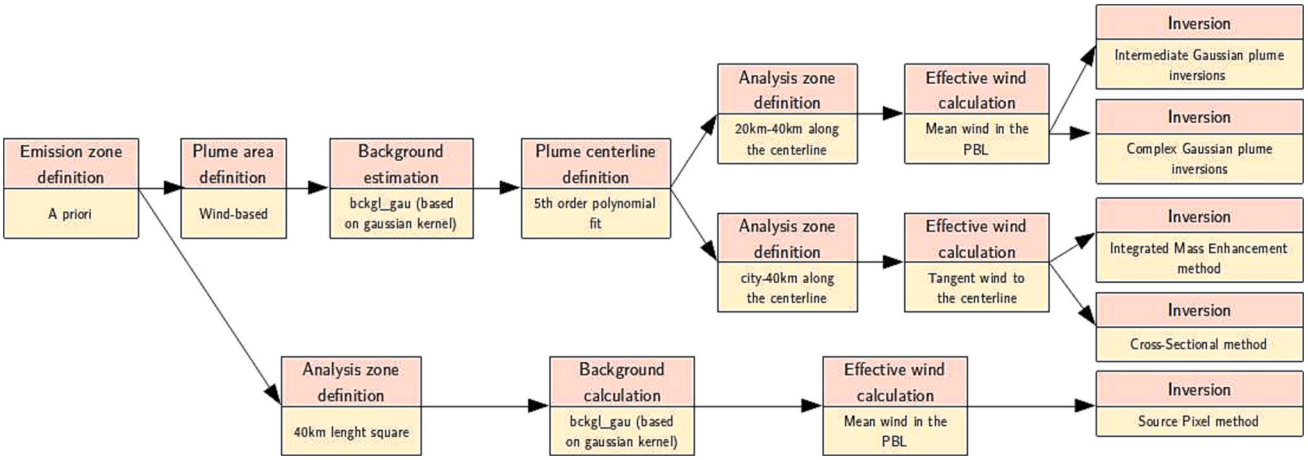

Fig. 8. Retained configurations for the emission estimation.

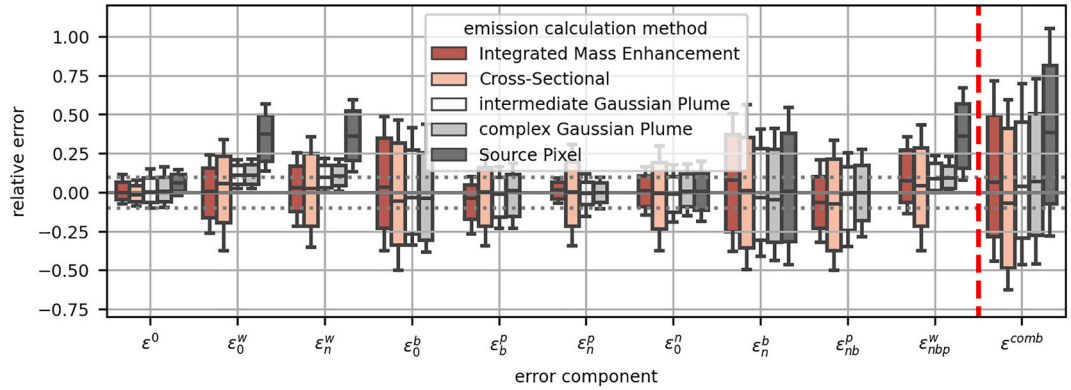

Fig. 9. Distribution of the error components when using the retained configurations for the emission estimation.

IQR (29–50%) when using the tangent wind method (with CS and IME inversion methods) or large bias (9–37%) when using the mean wind method (with the GP and SP inversion methods).

Unlike other methods, the SP method shows a large bias, which is due to the wind calculation step. The mean wind method accurately estimates the effective wind for analysis zones far from the city -where the CO_2 is well mixed- but not above the city and, therefore, not in the source area. This explains the high bias of the distributions of ε_0^w, ε_n^w and ε_{nbp}^w (and consequently ε^{comb}) when using the SP method.

4.5. *Influence of satellite spatial sampling*

This section analyzes how the distributions of the total error ε^{comb} and of the error components vary when the selected emission estimation configurations are applied to the realistic OCO-like observation samplings detailed in Section 2.3. When considering the OCO-2-samplings, we limit our analysis to the application of an adapted version of the CS method and of the GP2 inversion because the single-track sampling near the city does not allow for a plume centerline calculation (which is required for the GP3 inversion, for the IME method and for the strict application of the CS method detailed in Section 3.7) nor for a calculation of the CO_2 mass in the source area (and thus nor for the application of the SP method). The whole and undivided track is used as a single cross-section for the CS method and is, therefore, not necessarily perpendicular to the wind direction. Still, the principle of the background calculation, of the definition of the plume area along this section and of the flux calculation applies. All the cases when the meteorological situations are such that the plume does not cross the OCO-2 sampling are discarded from the computations and error statistics. In principle, applying the SP, CS and IME methods could require some image gap-filling to account for the loss of mass associated to the loss of pixels in the analysis zone due to cloud cover or quality control (Kuhlmann et al., 2020). However, we do not study this problem nor apply any gap-filling. Indeed, it would increase the complexity of the study and we expect that it would have a weak impact on the results here by considering the low number of observation pixels lost within the selected samplings.

Fig. 10 shows the distributions of errors for each tested track as a function of the inversion method. The distribution of ε^0 when using the OCO-3 samplings is similar to that when using the WRF grid (the absolute bias and IQR of this error are inferior to 5% and 20%) except when using the IME method (with which the bias is around -16%). The underestimation of the emissions of the core urban area obtained with the IME method may be due to the limited extent and asymmetric shape of the OCO-3 samplings. Indeed, this limited extent sometimes restricts the edges of the analysis zone, resulting in a loss of a significant part of the plume mass, and therefore an underestimation of emissions. The asymmetrical shape, meanwhile, perturbs our centerline definition: the derived centerline is slighty over-curved, resulting in an overestimation of the plume length and hence an underestimation of emissions. The errors obtained with the other inversion methods are slightly larger when using the OCO-3 samplings than when using the full WRF grid. The smaller number of points in OCO-3 samplings compared to the WRF grid enhances the impact of the measurement noise and thus increases the IQR of the error distributions. The IQR of ε^{comb} (Table 3) increases by 10

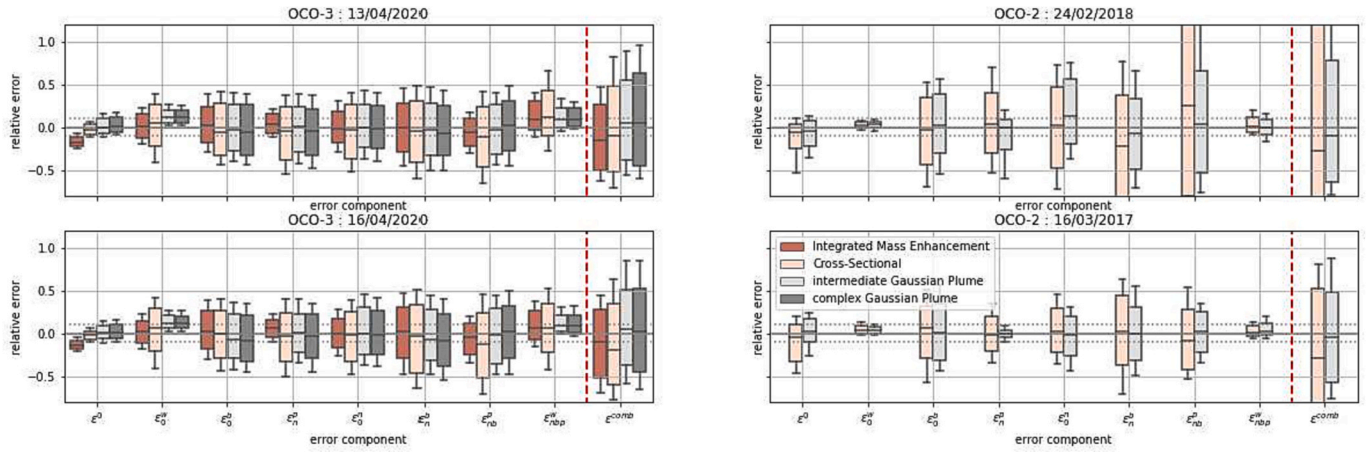

Fig. 10. Summary of the different error distributions when using OCO-3 (left panels) and OCO-2 (right panels) samplings.

Table 3
Total error (ε^{comb}) for the different samplings and inversion methods. The median and the 1st and 3rd quartiles are shown.

	WRF-grid	OCO-3	OCO-2
IME	+7% [−29%,+50%]	−12% [−52%, +28%]	–
CS	−7% [−48%,+41%]	−15% [−58%, +41%]	−28% [−118%,+101%]
GP2	+4% [−29%,+45%]	+5% [−38%,+53%]	−5% [−63%,+66%]
GP3	+7% [−28%,+51%]	+3% [−44%,+57%]	–

to 23% for the CS, GP and SP methods when using the OCO-3 samplings compared to when using the WRF-grid sampling. For the IME method, the IQR of ε^{comb} with the OCO-3 samplings is close to the IQR obtained with the WRF grid sampling (<2% difference) but its bias, as for ε^0, is larger with the OCO-3 sampling.

The IQR of the distribution of ε^0 is larger when using OCO-2 samplings (over 35% whereas it is inferior to 20% for OCO-3 samplings), as the cross-section of the plume is far from the city in the selected sampling cases. The difference between the results obtained when using the two OCO-2 samplings can be explained by their different distances to the city center but also by the loss of the data due to quality control or cloud cover in the South-West fringe of one of the two track sampling. This highlights the need for gap-filling or rejecting results from the CS and IME methods when the plume is observed with a sparse sampling. The smaller IQR of the ε_0^w distribution when using the OCO-2 samplings rather than the OCO-3 samplings or the full WRF grid is due to the accuracy in the wind estimation method over analysis zone far from the city (see Section 4.2). However, this does not compensate for the poorer results from the emission estimation methods with analysis zones far from the city, nor the degraded results in the background estimation due to the small size of the sampling area when using the OCO-2 samplings.

The typical total error amount to 6% [−34%,47%] with the WRF sampling, −5% [−48%,45%] with OCO-3 and − 17% [−91%,84%] with OCO-2 (Table 3).

5. Discussion

5.1. Impact of the errors in the 3D wind field

In Section 4.2 (and Appendix B.2), we estimate the errors in the emission estimates that are associated to the uncertainty in the derivation of the effective wind from a given 3D wind field. However, in the corresponding analysis with pseudo-data, the computation of the effective wind field can rely on a perfect knowledge of the true 3D wind field. When analyzing real data, one has to rely on 3D wind field from model simulations of from reanalysis products like ERA5, which can bear significant errors, especially when considering the urban scales (Lian et al., 2021). Errors in the 3D wind field products yield additional errors in the effective wind estimate, in the plume definition and, consequently, in the background estimates. Therefore, in this new section, we aim to provide insights on the emission estimation errors that are due to errors in the 3D wind field products used for the derivation of the effective wind in real conditions. Previous studies have used plume perturbation techniques (Ye et al., 2020), model comparison (Lei et al., 2021), or ensembles of simulations to estimate wind model errors (Díaz-Isaac et al., 2018). However, producing a well-calibrated ensemble remains challenging unless considerable computing resources are available to generate a sufficiently large ensemble of perturbed simulations. Furthermore, errors in wind fields differ across analysis products. As a first step, we perform here a simple evaluation of the impact of errors in wind speed and wind direction on emission estimation errors.

A spatial bias in the wind speed would only affect the calculation of the effective wind speed, and emission estimates are proportional to the effective wind speed for all emission calculation methods. Taszarek et al. (2020) compared the ERA5 wind fields to rawinsonde observations and diagnosed average and root-mean-square misfits of respectively 0.35 m/s and 1.93 m/s in the first kilometer of the atmosphere. The median value of the wind speed distribution in our WRF-Chem simulations of the Paris area is of 11 m/s. Assuming that the typical values of errors in wind analysis from Taszarek et al. (2020) apply to analysis and simulations over the Paris area and that the typical value of the wind speed from WRF-Chem is well representative of the wind speed over Paris, we get a typical relative error on the effective wind, and thus on the emission estimate for Paris, with a bias under 5% and a standard deviation of ≈20%.

In order to evaluate the additional uncertainties from spatial biases in the wind direction in wind fields used to analyze the XCO_2 images, we conduct a specific set of sensitivity experiments. In these experiments, we apply a random and spatially homogeneous rotation (one angle per image) to the true wind vector. The rotation for each image is sampled from an unbiased and normal distribution whose standard deviation is varied as a function of the experiment across the following values: 0°, 10°, 20°, 25°, 30°, 35°, 45°, 60° and 90°. This set of standard deviations corresponds to the range of standard deviations found by Deng et al. (2017); Feng et al. (2016); Lian et al. (2018) (see below). In each experiment, the resulting wind field is used for the estimation of the emissions with the optimal configurations of the GP2, GP3, CS and IME methods.

Fig. 11 illustrates the results from these sensitivity experiments, characterizing the impact of the spatial biases on the wind direction in terms of variations of ε^{comb}, of the background error (see Section 4.2) and of the ratio between the number of pixels of the true plume that have

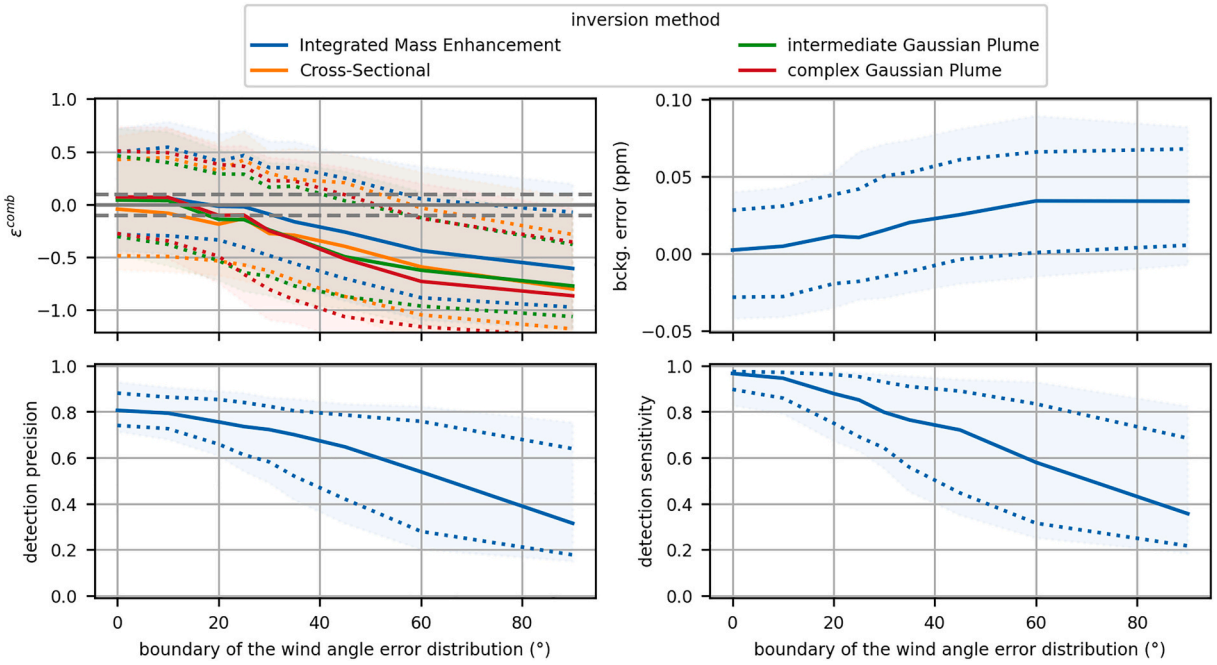

Fig. 11. Evolution of the distributions (median in plain line, 1st and 3rd quartiles in dotted line, 15.9–84.1% quantiles range in colour) of the detection precision, detection level, background error and ε^{comb} as a function of the wind direction error. ε^{comb} is shown for the IMECS, GP2 and GP3 methods.

been detected and (i) the number of pixels in the real plume (denoted detection sensitivity) or (ii) the number of pixels in the detected plume (denoted detection precision). The distributions of ε^{comb}, of the background error, of the detection sensitivity and the detection precision do not vary significantly as a function of the spatial bias in the wind direction long as the standard deviation of this bias is lower than 15°. However, when this standard deviation exceeds 25°, the plume definition misses large fractions of the true city plume. A direct consequence is the over-estimation of the background concentration (part of the signal from the city being analyzed as part of the background field) and thus the under-estimation of the emissions from the Paris core urban area.

Lian et al. (2018) compared measurements of surface wind direction above the Paris region to ECMWF high-resolution operational forecasts (HRES) with the Integrated Forecasting System (IFS) at 3-h resolution and to WRF simulations assimilating the meteorological observations. They show 5–8° biases and 41–47° RMS misfits between these meteorological analysis and the measurements. However, other studies comparing surface wind observations to wind directions modeled with

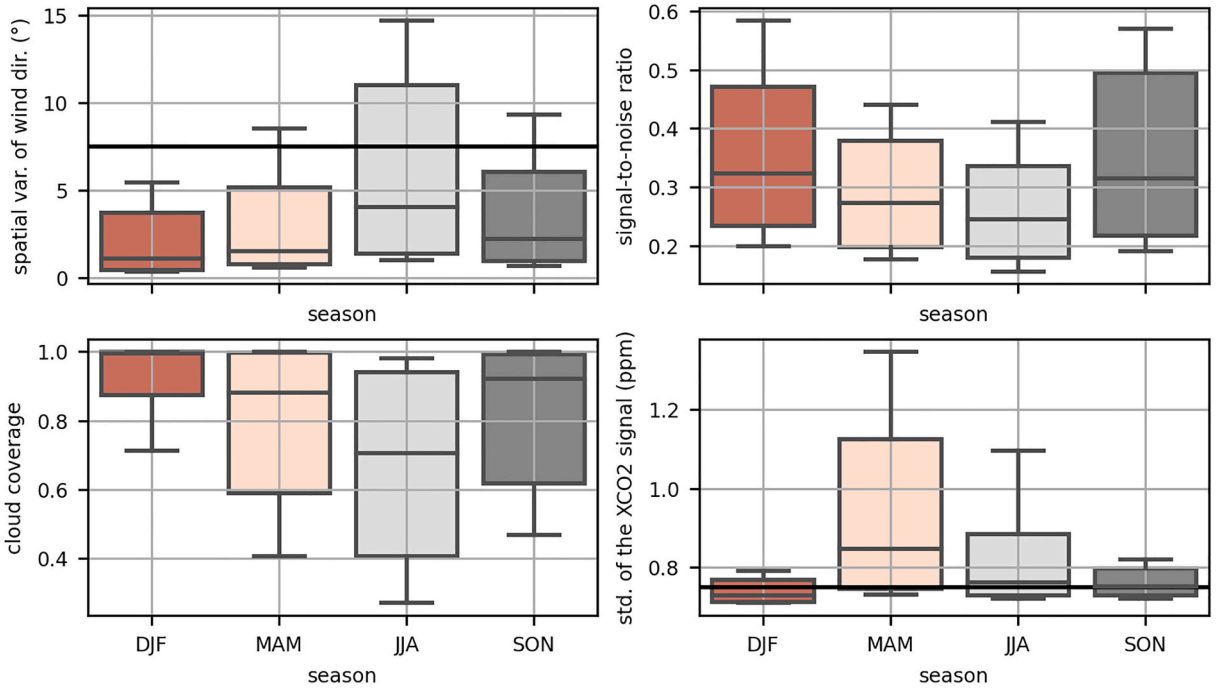

Fig. 12. Seasonal variations of the spatial variability of the wind direction, of the XCO_2 signal-to-noise ratio, cloud coverage and standard deviation of the XCO_2 signal in the image for the year 2018 as simulated by WRF.

WRF typically found few ° biases and approximately 25° RMS misfits (Deng et al., 2017; Feng et al., 2016) Whereas the impact of the errors in the wind field product diagnosed by Lian et al. (2018) would be important (leading to emission underestimates of 20–40%) the impact of the errors diagnosed by Deng et al. (2017); Feng et al. (2016) would be relatively small. Therefore a more systematic characterization of the impact of wind direction errors from re-analysis wind products in urban areas is needed.

5.2. Monthly dependency of the results

The precision of the emission estimation methods is sensitive to the spatial variability of the wind direction on the one hand and to the ratio of the average plume signal over the background variability (called signal-to-noise ratio in the following) and the standard deviation of the XCO_2 signals on the other hand. Fig. 12 shows the seasonal variations of these three parameters. We also show the variations of the proportion of cloudy pixels (i.e. pixels with cloud fraction >1%, threshold defined following Kuhlmann et al. (2019)).

During Summer, emissions decrease due to low energy consumption and reduced activity (summer vacation) in cities in the temperate mid-latitudes, such as Paris. Hence, the correlation between the signal-to-noise ratio and the standard deviation of the XCO_2 signals decreases. However, our filtering of the images when background conditions are not favorable to the emission estimation (Section 4.3) is based on the standard deviation of XCO_2 signals only. We need to reconsider this selection criteria, especially if analyzing images over different cities.

Following any of the criteria for good observation conditions (standard deviation of the XCO_2 signal, spatial variation in wind direction and the signal-to-noise ratio), the best seasons for the estimations of the emissions from Paris are Winter and Fall. Indeed, Spring and Summer seasons are impacted by a high variability of the wind directions, low signal-to-noise ratios, and high standard deviation of the XCO_2 signals. However, Winter and Fall correspond to higher cloud coverage, reducing the number of usable satellite images over Paris.

5.3. Potential error sources not taken into account

Our current analysis considered measurement error estimates from previous studies, hence directly dependent on satellite instruments, processing algorithms, and calibration procedures. The value of 0.7 ppm corresponds to empirical error estimates from Worden et al. (2017), similar to the expected CO2M measurement errors (Sierk et al., 2021). We assumed here that XCO_2 measurements are bias-free, thanks to a re-calibration of OCO-2 data using Total Carbon Column Observing Network (TCCON) XCO_2 measurements as reference (Wunch et al., 2017). However, residual biases remain in the OCO-2 retrievals (<0.4 ppm) depending on latitude, surface properties, and scattering by aerosols. Local biases (i.e., aerosols and surface properties) might degrade further our current flux uncertainty estimates. On the opposite, regional biases affecting retrievals at larger scales are removed by our approach. We also assumed that measurement errors were uncorrelated spatially due to a lack of detailed characterization at fine scales in the current literature. Ongoing work will help quantify potential error correlations in OCO-3 SAMs data caused by aerosol plumes, topography, and spatial patterns in surface characteristics (esp. albedo), which generate non-linearities and spatial error correlations at high resolution.

Cloud and aerosol filtering leads to partial data loss within observation sampling areas and, thus, in the analysis zone. While the GP inversion techniques, as defined here, can adapt to such cases, applying the direct flux integration methods may require some gap-filling of the XCO_2 image to avoid negative biases in the emission estimates (Kuhlmann et al., 2019). If the data loss is limited (as in Section 4.5), gap filling could be straightforward but its impact would be limited. When the data loss generates significant gaps resulting in relatively sparse sampling across the analysis zone, the choice and configuration of the gap-filling method could significantly impact on the emission estimate and, in any case, raise new uncertainties. Applying such gap-filling techniques, and assessing the various methods with their associated uncertainties (Gerber et al., 2018) is thus a complex topic that we did not address in this study and will require extensive tests and analyses.

Recent studies have shown that data loss in current OCO missions is about 85% over the largest 70 cities of the world (Lei et al., 2021). The vast majority of this loss is due to clouds and aerosol filtering. Based on Fig. 12, we note here that the amount of available data from satellite missions is anti-correlated with XCO_2 precision within each image, with high coverage but lower precision in Summer, and low coverage but higher precision in Winter (in the northern Hemisphere). This result suggests that flux uncertainties at longer timescales will be affected by the lack of data during cloudy months, partially compensated by less variable winds during cold months (higher precision per image).

A recent study by Ciais et al. (2020) estimated the contribution of human respiration. They concluded that for cities producing plumes of CO_2 detectable from space, human respiration represents a source to the atmosphere of 0.32 Gt CO_2 per year, compared to 10 Gt CO_2 per year of fossil fuel CO_2 emissions. Therefore, we neglected this term in our calculation. For real-data analyses over dense megacities such as New York City or Karachi, we expect human respiration to increase our uncertainty estimates by a few percent.

5.4. Perspectives for the use of complex transport models

Some inversion approaches rely on Eulerian or Lagrangian transport models (that are much more complex than Gaussian models) to quantify urban emissions (Lei et al., 2021; Wu et al., 2018; Ye et al., 2020). These models account for the variations of topography, emissions and wind, while our inversion methods assume that emissions and transport are stationary and, to some extent, homogeneous. Therefore, in principle, inversion approaches relying on Eulerian or Lagrangian models could provide more accurate emission estimates than our methods by relying on a better modelling of emission and transport conditions.

However, first, we have seen in Section 3.10 that the analysis areas we study correspond to a transport time of less than two hours in the vast majority of cases. This is a first limitation to the advantage of overcoming the assumption that emissions and winds are stationary when using complex transport models. Second, the ability to simulate the emission and transport variability does not ensure the ability to catch the actual variations of the emission and transport behind a given XCO_2 image with the Eulerian and Lagrangian model. The traditional inverse modelling techniques lack of flexibility when using these transport models, and can be highly impacted by the large transport modelling errors associated with the comparison between an XCO_2 image at a given time and the corresponding model simulation of the CO_2 field at this time (Feng et al., 2016; Lian et al., 2018). In particular, these techniques often assume that the simulations of the plume location and shape are accurate, and that the model errors can be summarized by a noise without temporal and spatial correlations (Broquet et al., 2018). The traditional pixel-wise comparisons between XCO_2 simulations and images can lead to problematic double penalties (Vanderbecken et al., 2023) which can raise much larger concerns than the assumptions of stationarity.

Recent analysis of plume transects by OCO-2 (Lei et al., 2021; Ye et al., 2020) have compared the integral of the signal of the plume detected and extracted from the OCO-2 observations to the integral of the signal from the neighbor sources simulated by the model, which mitigates the issue. However, such an approach requires the application of some of the most critical pre-processing steps of our methods, with the impact of one of the main source of errors in the emission estimations identified in this study: the estimate of the background field. This limits the capability to exploit the advantages of using Eulerian or Lagrangian transport models. Furthermore, the Eulerian and Lagrangian transport models are driven by the same type of meteorological fields as those

used for the flux computations in our light estimation methods. Therefore, comparisons between amplitudes of modeled and observed plume patterns when these modeled and observed patterns have not the same location may not necessarily be more robust than the direct computation of fluxes from the observed patterns with these meteorological wind fields. Finally, (Feng et al., 2016; Lian et al., 2018) have shown that the local XCO_2 fields from strong sources are generally poorly modeled by such transport models under low wind conditions (and hence, generally, when the spatial variability of the wind direction is high), i.e. when the assumptions underlying our estimation methods are challenged and when these methods yield high errors on the emission estimates.

Hence, the uncertainties in the background and the wind spatial variations, which have been identified in this this study as the main sources of errors for our estimation methods, impact to a similar extent the current inversion methods relying on complex transport models. This can explain why the few studies which have compared the different types of inversion methods (such as Lei et al. (2021)) did not show significant differences between them. In such a context, the low computational cost of our estimation methods reveals to be a critical advantage over the methods using complex models. However, lighter and more flexible inverse modelling methods relying on Eulerian or Lagrangian transport models (e.g. based on machine learning techniques) will likely emerge, and are already studied (Dumont et al. 2023). Such methods could exploit the advantages and realism of the transport models without using a specific model simulation as a strong constraint for the analysis of a specific image. This could redraw the comparisons to the light estimation methods analyzed here.

5.5. Further development and generalization

As shown in previous studies, the estimation of CO_2 emissions over urban areas remains complex and impacted by large uncertainties (IQR≈75%, standard deviation ≈70%). The uncertainties found in our study are slightly higher than those found by Kuhlmann et al. (2020) over Berlin (40–53%) and higher than Nassar et al. (2017) using OCO-2 data (single tracks) near a power plant. In the case of power plants studied by Nassar et al. (2017), the local enhancements are one order of magnitude larger than Paris' (i.e., a few ppm) and the plumes are thinner, which can explain the better results. Kuhlmann et al. (2020) show simulations in which the distinction between the plume from Berlin from its background appears to be slightly clearer than that between the plume from Paris and its background in our simulations. Their typical plume enhancement is 1 ppm. This could explain why they derive uncertainties in their emission estimates that are smaller than ours. However, both studies highlight the challenge of getting accurate urban emissions estimates.

The IQR of the total error appears to be too large (>70%) to evaluate urban emission from a single image, despite the low bias in error distribution (<10%). A large number of images is thus necessary to obtain sufficient precision to monitor policy-relevant trends (typically around 2–3% of the emissions per year for most megacities worldwide). We found only 7 SAMs over Paris with >1500 usable pixels between 2019 and 2021 (a period corresponding to approximately 20 months of data). Therefore, OCO-3 SAMs will provide a unique dataset to quantify the value of XCO_2 measurements. Still, only a handful of cities with high emission trends might be selected to demonstrate emissions monitoring potential from space.

However, we emphasize that the two pre-processing steps responsible for a large fraction of the total errors (i.e., wind and background calculation) could benefit from novel image processing techniques. This will benefit computationally-light methods and model-based inversions (Wu et al., 2018; Ye et al., 2020), especially when the simulations do not integrate biogenic flux contribution.

Our analysis of the various light emission estimation techniques and our optimization of their configurations is based on experiments over a single city. In principle, the specific emission and transport conditions corresponding to our Paris case could guide some of our conclusions, particularly when analyzing the optimal values of certain parameters in the pre-processing steps, e.g. the specific distances for the analysis area, the threshold on wind variability used to select images. Most of the conclusions regarding the techniques (concerning plume detection, background or effective wind estimation, the reasoning for the analysis area) and many of the typical values derived here should be independent of the city targeted by the emission estimation. However, major exceptions may apply to cities with complex regional topography (e.g. in deep valleys) and to coastal cities. Finally, the typical error levels obtained here should highly depend on the amplitude and spread of the city emissions. A next step of the analysis of the light urban CO_2 emission estimation methods, or their applicability and of their accuracy depending on the observation systems should thus be associated with their application to a wide set of cities.

6. Conclusion

In this study, we characterized the uncertainties in the emissions estimates from a large urban area based on the application of computationally-light inversion methods -Integrated Mass Enhancement, Cross-Sectional, Source Pixel, and Gaussian Plume inversions- to XCO_2 satellite images. This assessment is based on pseudo-data experiments focused on Paris, with high-resolution XCO_2 images simulated with the WRF-Chem model. We decomposed the error of the emission estimation methods by gradually introducing the different sources of uncertainties to evaluate the importance of each pre-processing step in the total error and to select the most accurate techniques and configurations for each step. The error components were derived when using a full sampling of the area at 1-km spatial resolution and when using realistic observation samplings corresponding to OCO-2 and SAMs from OCO-3 in order to determine the influence of the sampling strategy on the results.

Using appropriate methods for estimating the key parameters for these estimation methods (plume area, background concentrations and effective wind speed, etc.), the Integrated Mass Enhancement, Cross-Sectional methods and two of the tested variants of the Gaussian plume model inversion give low bias (<10%) but high IQR (≈75%) errors on emission estimates when using the full sampling at $1km^2$ resolution. The Source Pixel method gives highly biased results in the tested configuration (38% bias and 89% uncertainty). Indeed, none of the methods used here to estimate the effective wind was a good estimator of the effective wind for the analysis zone used by the Source Pixel method. Using transport models to support the derivation of the effective wind (Varon et al., 2019) may overcome this issue but would cancel the advantage of using such a low computational emission estimation method.

When using their best configurations, the Integrated Mass Enhancement, Cross-Sectional, and Gaussian Plume inversions provide similar errors, and the main sources of uncertainties for all methods appear to be, first, the calculation of the background concentration underlying the targeted plume and secondly, the computation of the effective wind driving this plume. We highlighted a sensitivity of the error distribution to wind meteorological conditions (namely, to the spatial variability in the wind direction) and to the spatial variability in the background XCO_2 field. The main sources of errors when using the computationally-light emission estimation methods are thus shown to be shared by the current inversion methods relying on Eurlerian or Lagrangian transport models, so that the typical level of uncertainties diagnosed here for the estimates of the emissions from Paris should apply to the current plume inversions techniques in a general way. The analysis of the results with realistic observation samplings corresponding to OCO-3 SAMs showed a slight increase of the error IQR (≈ +20%) due to the coarser sampling.

Author contributions

A.D., G.B. and T.L. designed the study. A.D. did the coding, analysis for the manuscript. Sections 5.3 and 5.5 were written by T.L. and the others by A.D. and G.B. in collaboration. J.L. designed and ran the WRF-Chem simulations and gave precious advice on the synthetic data. F.-M. B. provided general feedback and opinions on manuscript and research directions. All authors gave valuable comments and revisions to the final paper.

Declaration of Competing Interest

The authors declare that they have no known competing financial interests or personal relationships that could have appeared to influence the work reported in this paper.

Data availability

The authors do not have permission to share data.

Acknowledgments

We thank Origins.earth and Hervé Utard who kindly provided the inventory used for the simulations. OCO-2 and OCO-3 retrievals, used to defined the realistic samplings, were produced by the OCO-2/3 project at the Jet Propulsion Laboratory, California Institute of Technology and obtained from the OCO-2 and OCO-3 data archives maintained at the NASA Goddard Earth Science Data and Information Services Center (https://disc.gsfc.nasa.gov/). We thank Annmarie Eldering, former Project Scientist in OCO-2 and 3 missions, for her help and advice with the OCO data. This work was supported by CNES with the funding of the OCO-3-city project. T. Lauvaux was supported by the Make Our Planet Great Again (MOPGA) fellowship program (CNRS, project CIUDAD).

This work was supported by the CNES (Centre National d'Etudes Spatiales), in the frame of the TOSCA OCO-3-city project.

Appendix A. Complement on the methododology

A.1. Section 3.1: definition of the plume area

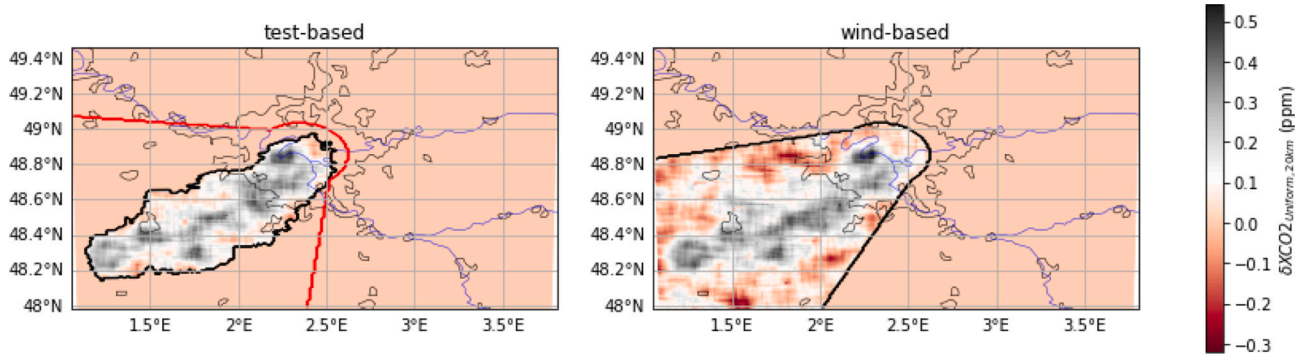

Fig. S1. Illustration of the test-based and wind-based plume definition methods on December 1st 2019 at 10 am. The black line indicates the contour of the plume defined with the corresponding method. The red line on the left panel indicates the restricted zone.

A.1.1. Test-based methods

A preliminary estimate of the background (denoted $XCO2_{bckgp}$), is derived based on the analysis of the whole image for such a test. We test different options for this derivation: computing the mean (bckgp_mean) or the median (bckgp_med) of the concentration in the image, fitting a subset of this concentration field (from which the part downwind of the city as been removed) with a plane (with a bilinear function; bckgp_2df) or extracting the average concentration over an upwind zone defined based on the location of Paris and by the mean wind in the PBL over this location (bckgp_upw). This background estimate is subtracted from the data. For each pixel of the image, we define a neighborhood as a square of size N km, we apply a smoothing function over this neighborhood and we use the resulting value for the pixel for the statistical test. We test the hypothesis that this resulting value can correspond to the sum of an enhancement of concentration above the background in the smoothed plume and of the average of the observation noise over the neighborhood, whose standard deviation is σ_{meas}. In practice, we test the hypothesis that this resulting value can be a sample of a normal statistical distribution whose mean is superior or equal to zero, and whose standard deviation corresponds to $\sigma_{meas}/\sqrt{(n_{px})}$ (with n_{px} being he number of pixel in the neighborhood). Here we neglect the uncertainty in the smoothed XCO_2 field associated to the background. We define the pixels for which the probability to belong to the plume is high as those passing the test with a 99% confidence:

$$z(x,y) = \frac{\delta XCO2_{sm,N}(x,y)}{\sigma_{meas}/\sqrt{n_{px}}} > 2.33 \quad (2)$$

where $\delta XCO2_{sm,N}$ corresponds to the smoothed field of $XCO2 - XCO2_{bckgp}$. Different smoothing functions are tested: the mean or the median, of the application of a Gaussian or wiener filter within the neighborhood. We also test different values for N ranging from 10 km to 30 km with a 10 km step. $\sigma_{meas}/\sqrt{(n_{px})}$ is the noise on the mean concentration over the neighborhood. The normalization based on this noise is consistent with the smoothing based on the average of the data over the neighborhood. The statistical noise on the resulting value for the pixel that is investigated with other smoothing methods is different. We nonetheless use such a normalization in all cases. The analysis of results in section B.3 indicate whether this can raise significant errors in the plume definition. For the tests where we do not put noise on the observations, the test becomes: $z(x,y) =$

$\delta XCO2_{sm,N}(x,y) > 0$.

Pixels that are not labeled but that are enclosed within a cluster corresponding to the city plume are integrated into this plume area. The points that are at >45° downwind of the city using the direction of the mean wind in the PBL are labeled as not being part of the plume (see Fig. S1). When no plume is detected in the image, no emission calculation is made. Each combination of one method for the computation of the preliminary background, of one smoothing length N, and of one smoothing function corresponds to an individual plume definition configuration.

A.1.2. Wind-based methods

The plume is defined as the points that are at <22.5° downwind of the city using the direction of the mean wind in the PBL (see Fig. S1).

A.2. Section 3.3: Background estimation

The six methods can be listed as:

- 'bckgl_mean': computation of the average of the concentrations in the plume (when using the GPs, IME and CS inversion methods) or source area (when using the SP inversion method) edge;
- 'bckgl_upw': computation of the average XCO_2 values in an area upwind the plume defined based on the location of Paris and by the mean wind in the PBL, not computed for the SP method as it would be the equivalent to the 'bckgl_mean' method in this particular case;
- 'bckgl_2df': derivation of the plan which best fits the concentrations in the plume or source area edge;
- 'bckgl_cs': a method that can be seen as an extension of Ye et al. (2017) for a 2d image. It relies on a preliminary computation of the plume centerline and on a preliminary definition of plume cross-sections orthogonal to this centerline (see sections 3.4 and 3.5) and is thus not used with the SP method. The background field is derived as the combination of background estimates on each cross section. These estimates are derived as the linear functions of the positions along the cross sections which best fit the XCO_2 concentrations in the plume edges;
- 'bckgl_bih': a method using a technique of image restoration by inpainting the values within the plume or source area limits with biharmonic equations (see https://scikit-image.org/docs/stable/api/skimage.restoration.html, last access March 21rt 2022). The smoothed XCO_2 field ($\delta XCO2_{sm,N}$) outside the plume or upwind of the source area is used to calculate the coefficient of the biharmonic equations.
- 'bckgl_gau': adaptation of the method used in Kuhlmann et al. (2020). It is also based on the smoothed XCO_2 values. It interpolates the smoothed XCO_2 values from outside the plume with a 2D Gaussian kernel to get the background values in the plume area. The size of the kernel used here differ from that used in Kuhlmann et al. (2020). We choose to use a relatively small kernel size (4 pixels) to conserve as much as possible the local structure of the background. However this required the use of an iterative process to cover the whole plume area since the plume size is often larger than the kernel size in our study case (even when the kernel size is 10 pixels large as in Kuhlmann et al. (2020)), while Kuhlmann et al. (2020) did not face such a problem.

A.3. Section 3.6: Effective wind evaluation

A.3.1. Calculation of the effective wind of reference

The effective wind is defined as the vertically integrated wind driving the XCO_2 field: its vertical integration must be ponderated by the vertical distribution of CO_2 as follows:

$$\overrightarrow{W}_{eff}(x,y) = \frac{\sum_z \overrightarrow{W}(x,y,z) * u^{anth.}_{CO_2}(x,y,z) * \Delta P_{dry}(x,y,z)}{\sum u^{anth.}_{CO_2}(x,y,z) * \Delta P_{dry}(x,y,z)} \quad (3)$$

where $\overrightarrow{W}(x,y,z)$ is the wind field, $u^{anth.}_{CO_2}(z,x,y)$ is the CO_2 dry air mole fraction signal associated to the anthropogenic emissions from Paris core urban area and $P_{dry(z,x,y)}$ is the dry air pressure. Eq. 3 is used to derive the actual effective wind field. However, since the spatial (vertical and horizontal) distribution of $u^{anth.}_{CO_2}$ is not known for the analysis of the images, an approximate estimate of the effective wind must be derived based on the distribution of $\overrightarrow{W}$. The impact of the uncertainty in the knowledge of this wind field is ignored in this study and we use, for the analysis of the images, a perfect knowledge of the full $\overrightarrow{W}$ field from WRF-Chem (in tests corresponding to situations for which inversion methods rely on the full wind field from meteorological analysis) or of its surface value: $\overrightarrow{W}_{10m}(x,y) = (U_{10m}\ \ V_{10m})^T$ (in tests corresponding to situations for which inversions rely on wind data from surface stations).

A.3.2. Description of the effective wind methods

Three different methods of vertical integration or sampling are tested to compute the effective wind. The methods derive it as a 2D field ($W_{eff}(x,y)$) before aggregating it as a single value (W^{av}_{eff}). First, at each location (x,y), they rely on:

- the average, weighted by the dry air mass, of $\overrightarrow{W}$ in the PBL, method which assumes that the plume can rapidly mix downwind to the city.
- the use of the surface wind (10 m above the surface) multiplied by a scaling coefficient, following Varon et al. (2020). Here we fix the scaling coefficient to 1.8 which is the average ratio between surface wind and the actual effective wind field in the analysis zone '20 km–40 km'. The use of such a precise knowledge of this average ratio is an optimistic aspect of the corresponding test but the variations in space and time of this ratio challenges the use of the surface wind.
- The third method (denoted tangent wind in the following) take advantage of the 2D extension of the image and derive a "local" effective wind for each cross-section defined in section 3.5. First, it computes the local tangent to the plume centerline at the intersection with each cross-section. Then it computes the atmospheric level in WRF where the direction of the mean wind in the cross-section is the closest to the direction of this local tangent. The wind field in the cross-section at the computed level is used as the effective wind in the corresponding cross-section.

Finally, the methods average the effective wind horizontally in the analysis zone (resp. cross-section for the CS method and "source area" for the SP method), weighting the average by the smoothed XCO_2 values ($\delta XCO2_{sm,N}$). The smooth XCO_2 field is the one calculated at the plume definition step when the plume has been defined with a test-based method. Otherwise, for the wind-based method or when the plume is known, the smoothing is made with the uniform method at a 20 km scale. The notation $\overrightarrow{W}_{a.z.}$ (resp $\overrightarrow{W}_{c.s.}$, $\overrightarrow{W}_{s.p.}$) is used in the following.

A.4. Section 3.7: Inversion methods

All our computation of the emissions apply to the field of enhancement of the total CO_2 mass in the vertical columns column (in g/m^2) associated to the signature of the city emission in the XCO_2 field:

$$\Delta\Omega(x,y) = \frac{M_{CO_2}}{M_{\text{dryair}}} * \Delta XCO2 * 10^{-6} * \frac{P_{\text{dryair}}(\text{surface})}{g} \tag{4}$$

where g is the Earth's gravity and $P_{\text{dryair}}(\text{surface})$ is the dry air surface pressure, calculated as $P_{\text{dryair}}(\text{surface}) = \sum_z q_{dry}(x,y,z) * \Delta P(x,y,z) + P_{top^*} < q_{dry}(x,y,z_{imax}) >_{x,y}$, where the relative humidity q_{dry} and the pressure P are assumed to be perfectly known and are taken from the WRF-Chem simulations. The emission obtained with the method is denoted F_{sat} in the following.

A.4.1. IME

The IME method (Frankenberg et al., 2016; Varon et al., 2020) calculates the total mass present in the analysis zone and divide it by the estimate of the time of residence of the CO_2 molecules in this zone. This residence time is calculated as the ratio between the length of the plume centerline in the analysis zone L, and the speed of the effective wind (averaged in the plume analysis zone):

$$F_{sat} = \frac{\text{total } CO_2 \text{ mass in plume}}{\text{CO2 residence time in plume}} = \frac{\left|\overrightarrow{W}_{a.z.}\right|}{L_{IME}} * \int_{(x,y)\in plume} \Delta\Omega(x,y)\,dx\,dy \tag{5}$$

The definition of the plume length taken here differs from Varon et al. (2020).

A.4.2. SP method

The SP method (Buchwitz et al., 2017; Varon et al., 2018) follows the same idea as the IME method, except that it focuses on the enhancement of CO_2 due to the emissions just above the city. This method was mainly design for point sources, contained in one pixel of the satellite images, whereas its application to a city requires the use of a "source area" with a rough definition. We arbitrary fix the "source area" as a square of 40 km wide, roughly encompassing Paris core urban area. The time of residence in the source area is evaluated as the ratio between half the width of this square and the effective wind averaged over the "source area".

$$F_{sat} = \frac{\text{total } CO_2 \text{ mass in mega} - \text{pixel}}{\text{CO2 residence time in mega} - \text{pixel}} = \frac{<\Delta\Omega>_{\text{mega-pixel}} * L_{SP}^2}{0.5 * L_{SP} / \left|\overrightarrow{W}_{s.p.}\right|} = 2 * |\overrightarrow{W}_{s.p.}| * <\Delta\Omega>_{\text{control zone}} * L_{SP} \tag{6}$$

A.4.3. CS method

The CS method (Krings et al., 2011; Kuhlmann et al., 2020; Varon et al., 2019, 2020) directly computes the flux of CO_2 through the cross-sections of the plume. This flux is given by the product of the mass and the component of the effective wind speed perpendicular to the cross-section:

$$F_{sat}(i_{cs}) = \overrightarrow{W}_{c.s.} \cdot \overrightarrow{n}_{\text{cross-section}(i_{cs})} * \int_{x,y\in\text{cross-section}(i_{cs})} \Delta\Omega(x,y)\,ds(x,y) \tag{7}$$

where s is the abscissa of the projection of the pixel on the curvilign abscissa of the normal to the plume centerline at the center of the cross-section and $\overrightarrow{n}_{transect}$ the unit vector perpendicular to the cross-section. In theory the effective wind should be perpendicular to the cross-section, but errors in effective wind estimation and the uncertainty in the plume centerline detection make them often only nearly orthogonal.

Each cross-section gives a different estimation of the flux. The retained emission calculation for a given plume is the median of the flux given by the cross-sections in chosen the plume analysis zone. We thus retain only one estimation per plume for the method except in the first part of section 4.1 and Appendix B.1.1 where all cross-sections are studied individually in order to tune some of the method parameters (cross-section size, plume centerline method and plume analysis zone).

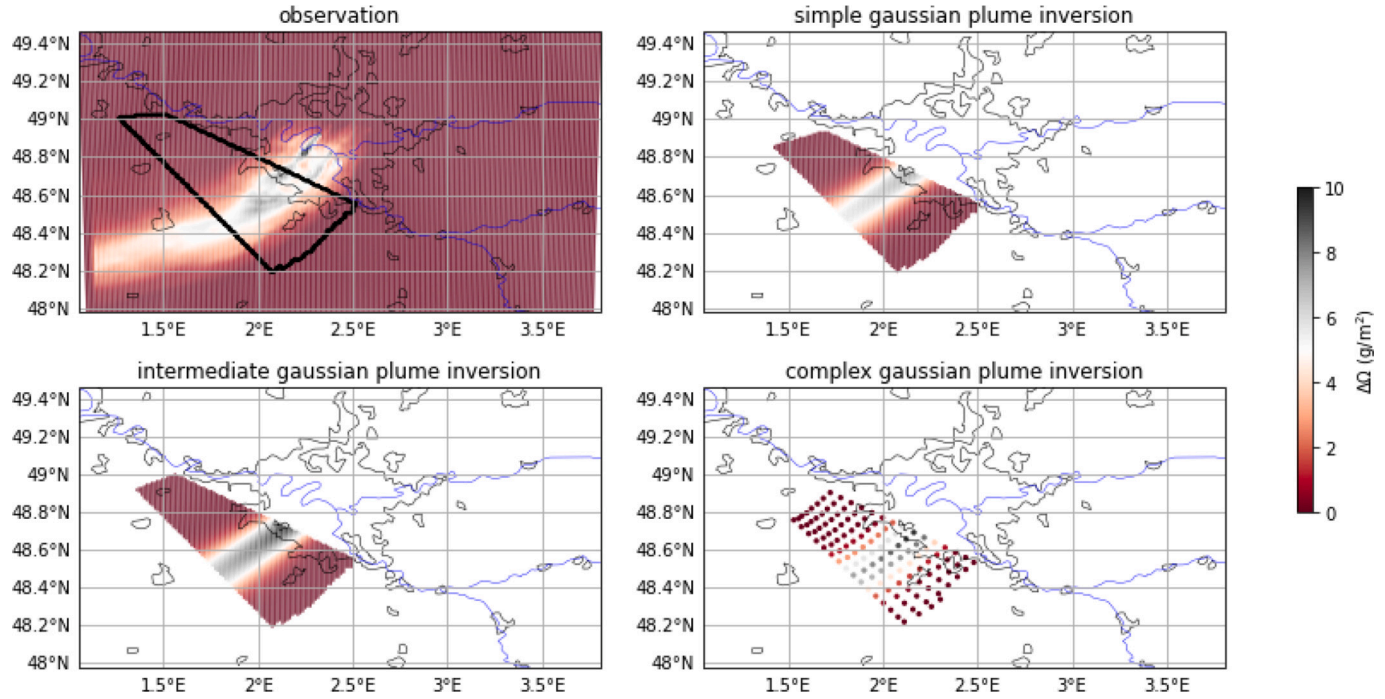

Fig. S2. Illustration of the simulated mass enhancements with the different Gaussian plume inversions on 1/12/2019 at 10a.m with the XCO_2 column and wind perfectly known. The black line on the upper left panel indicates the sampling zone.

A.4.4. Inversions using Gaussian plume models

The general formulation of the Gaussian models we use to simulate the plume from Paris and which applies to extended sources follow that of Krings et al. (2011):

$$\Delta\Omega_{gp}(x,y) = \frac{F}{\sqrt{2\pi} * \left|\vec{W}_{a.z.}\right| * \sigma_y(x)} e^{-\frac{y^2}{2*\sigma_y(x)^2}} \tag{8}$$

where the x and y-axis follow the directions along and across the effective wind, and where the origin of the coordinate system is the city center. The term $\sigma_y(s)$ allows to account for the horizontal extension of the source. We take $\sigma_y(x) = a*\left(x + \left(\frac{R_{Paris}}{4a}\right)^{1/0.894}\right)^{0.894}$ as Krings et al. (2011), where a is the Pasquill stability parameter.

The inversions consist in fitting the Gaussian plume models to the total column mass enhancement $\Delta\Omega$ derived from the XCO_2 images, the emission from the city F_{sat} being one of the parameters optimized for this fit.

We tested three variants of this approach with different Gaussian models and/or different set of parameters optimized by the inversion:

- the "simple Gaussian plume model" with inversions where the city radius is fixed at 20 km, the Pasquill parameter is computed following Pasquill (1961) and the wind direction is fixed as the direction of the effective wind estimated in section 3.6. The emission estimate is obtained by minimizing the sum of the square differences between the observed ($\delta\Omega_{sat}$(x,y)) and modeled mass enhancement ($\Delta\Omega_{gp}$(x,y)) over the whole domain. This minimization with respect to a single parameters, whose impact on the modeled mass enhancement is linear, is straightforward and computed analytically.
- the "intermediate Gaussian plume model" with inversions where the city radius, the pasquill parameter and the wind direction are not fixed and optimized together with the emission estimate. The cost function to minimize is still the sum of the square difference between the observed ($\delta\Omega_{sat}$(x,y)) and modeled mass enhancement ($\Delta\Omega_{gp}$(x,y)) but with a, θ and r being optimized along F_{sat}. The minimization is done using a classical minimization function of python's scipy package (see https://docs.scipy.org/doc/scipy-1.8.0/html-scipyorg/reference/generated/scipy.optimize.minimize.html, last access on on March 21st 2022).
- the "complex Gaussian plume model" whose central axis follows the plume centerline derived following section 3.4 with inversions where the wind direction is fixed but not the city radius and pasquill parameter, which are optimized together with the emission estimate. The non-regular grid defined in section 3.5 is used for the optimization of the parameters. The CO_2 mass enhancement corresponding to each portion of each cross-section is derived as the average of the CO_2 mass enhancements of the pixels in the portion. Eq. 8 is applied in the space defined by our irregular grid by replacing the (x,y) coordinates by the (s,n) coordinates in its formulation. The cost function to minimize is the sum of the square difference between the observed ($\delta\Omega_{sat}$ (s,n)) and modeled mass enhancement ($\Delta\Omega_{gp}$ (s,n)) fover the irregular grid with a and r being optimized along F_{sat}. The minimization is done using the same minimization function as with the intermediate Gaussian plume model.

For the intermediate and complex gaussian plume model, the initial value of F_{sat} (denoted F_{sat}^{init}) given to the solver is a random number taken in a beta distribution (with α=1.35, β=2.5 ad a scaling factor of 5) multiplied by the true emission of the core urban area. The choice of such distribution was made to have a sufficient spread without getting negative values. The distribution of the a priori values given to the solver has thus a bias of ≈60%

of the true emissions and an IQR of ≈165%. The initial values of the other parameters are fix to the one taken for the simple Gaussian plume model. The parameters are also scaled as follow: $X = \left(\frac{F_{sat} - F_{sat}^{init}}{F_{sat}^{init}} \quad \frac{a}{120} \quad \frac{\theta - \theta\left(\vec{W}_{a.z.}\right)}{\pi/4} \quad \frac{r - R_{Paris}}{R_{Paris}/2} \right)^T$ and are restricted as follow during the optimization: $F_{sat} \in [-F_{sat}; +\infty]$, $a \in [0; 240]$, $\theta \in \left[\theta\left(\vec{W}_{a.z.}\right) - \pi/4 ; \theta\left(\vec{W}_{a.z.}\right) + \pi/4\right]$ and $r \in [0.5{*}R_{Paris}; 1.5{*}R_{Paris}]$.

Fig. S2 shows an example of the simulations of the mass enhancements given by the three variants for the Gaussian models on the '20 km–60 km' analysis zone and their inversions 1/12/2019 and their comparison to the actual plume from Paris.

Appendix B. Analysis of the different error distributions

B.1. Analysis of the dependencies of the results to meteorological parameters when the plume, background and effective wind are known: selection of the test cases

This section details the results presented in section 4.1. We study the performance of the inversion methods with different parameters and their dependency to the meteorological conditions by looking at the error distributions ε^0 (sections B.1.1 and B.1.2) and ε_0^n (section B.1.3). The methods set aside in the main text are more deeply detailed and compared to document the choices made. The tests are performed with a perfectly known plume, background and effective wind.

B.1.1. Focus on the result of the decomposition of the CS method per cross-section

Fig. S3 shows the statistics of errors ε^0 corresponding to estimates from individual cross-sections, as a function of the distance from the city center to the cross-sections (the distance along the central axis to the nodes). The results are separated in four bins, corresponding to the quartiles of the spatial variability of the wind direction. We see that, in all panels, the IQR of ε^0 increases with the distance between the cross-section and the city center. The method becomes less precise over remote parts of the plume which correspond to a longer period of transport and thus to larger levels of atmospheric diffusion. However, the abrupt increase of the error IQR at 60 km from the city may be an artifact: at this distance of the city, some of the cross-sections are cropped by the image borders depending of the direction of the plume. The precision also decreases with the wind direction variability.

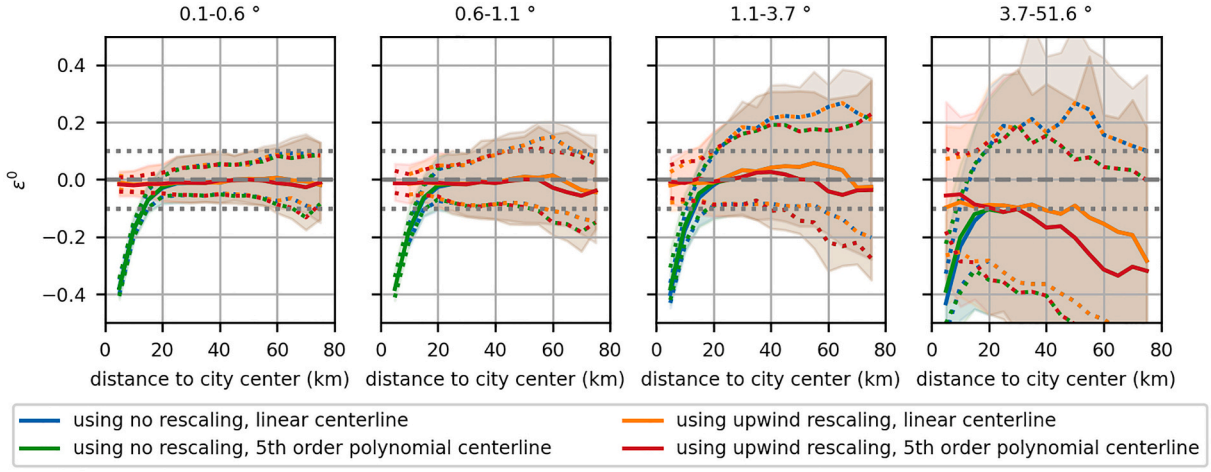

Fig. S3. Distribution (median in plain line, 1st and 3rd quartiles in dotted line, 15.9–84.1% quantiles range in colour) of the error ε^0 for estimates of the emissions per cross-section as a function of the distance between the cross section and the city center when applying the CS method. Each figure shows a binning of the result for a quartile of standard deviation of the spatial variability of the wind direction. Results are obtained with (blue, green) and without (orange, red) using the rescaling with the part of the core urban are upwind of the cross-section (as described in section 3.8), with a linear (blue, orange) or 5th order polynomial (green, red) fit for the centerline.

The Fig. S3 shows results with the rescaling of the emission estimates to account for the restriction of their emission zone described as the default emission zone in section 3.8 or when using the total instantaneous emission of the city to rescale the emissions. The results show that the restriction of the emission zone to the fraction of the city upwind of the track (default emission zone) decreases the bias for the the cross-sections at <20 km of the city center (i.e. above the core urban area) from values down to −40% to values between −2 and + 2%. Using the emission zone gives accurate results above the city without impacting the results for the cross-sections outside of the city limits. Thus, the default emission zone is used as the reference case in this study: therefore, in the following "not rescaled results" indicates that only the "default" emission zone is applied and "rescaled results" indicates that the tested emission zone described in the middle of section 3.8 is applied.

When the wind direction variability is below 1°, the sensitivity of ε^0 to the centerline calculation method is low. When this variability exceed 1°, and thus when the plume deviates significantly from a straight dispersion, results become sensitive to the computation of the centerline. For a wind direction variability comprised between 1,0 and 2,9°, better results (a smaller bias) are obtained when using a centerline based on a 5th order polynomial fit between 40 km and 60 km from the city center. However, the centerline based on a linear fit yields a smaller bias for a spatial variability of the wind direction larger than 2.9° at such distances. Rather than catching the main path of the plume, the 5th order polynomial fit could tend to

overfit some of its meandering over short distances from the city (because this is where the XCO_2 signal is the highest), while the linear fit keep on catching its mean direction. We choose to keep the method which give less bias for the favorable wind conditions (three first panels) and thus to focus on results given with the centerline fitted with a 5th order polynom in the following.

B.1.2. Analysis of ε^0

B.1.2.1. Sensitivity to the meteorological conditions. In general, all inversion methods give accurate results (low bias and low IQR) when the meteorological conditions favor the ventilation of the emitted CO_2 in a well developed and straight plume, i.e. with a high wind speed and a low variability of the wind direction (illustration is given by Figs. S3 and S4). However, when the CO_2 emissions accumulate over Paris or is evacuated within a very complex plume, situations characterized by large plume and high XCO_2 values, the results bear large errors. Those situations can be driven by low effective wind speeds or high variations in space (horizontally and vertically) and in time (over the few hours before the observation time) of the wind direction. Furthermore, the representativity of the instantaneous emissions diminish with the effective wind speed. The spatial variability of the wind direction is measured via the circular variance of the 3D wind field in the PBL at the observation time and the wind speed temporal variability is measured as the difference between the effective wind speed at the observation time minus the effective wind speed one hour before the observation time. The spatial variability of the wind direction, the effective wind speed, the strength of the XCO_2 signal, the size of the plume and the effective wind speed temporal variability are all correlated (correlation superior to 0.6 except with the XCO_2 signal strength where it is around 0.2).

Fig. S4 illustrates the distribution of ε^0 as a function of wind parameters for the selected estimation methods. An abrupt increase of the IQR and of the absolute bias of ε^0 can be seen for high spatial variability of the wind direction. Consequently, we decided not to apply the emission computation in the following of the study to cases corresponding to approximately the 15% highest values of the spatial variability of the wind direction (black vertical lines on Fig. 6). The threshold value is fixed to 7°.

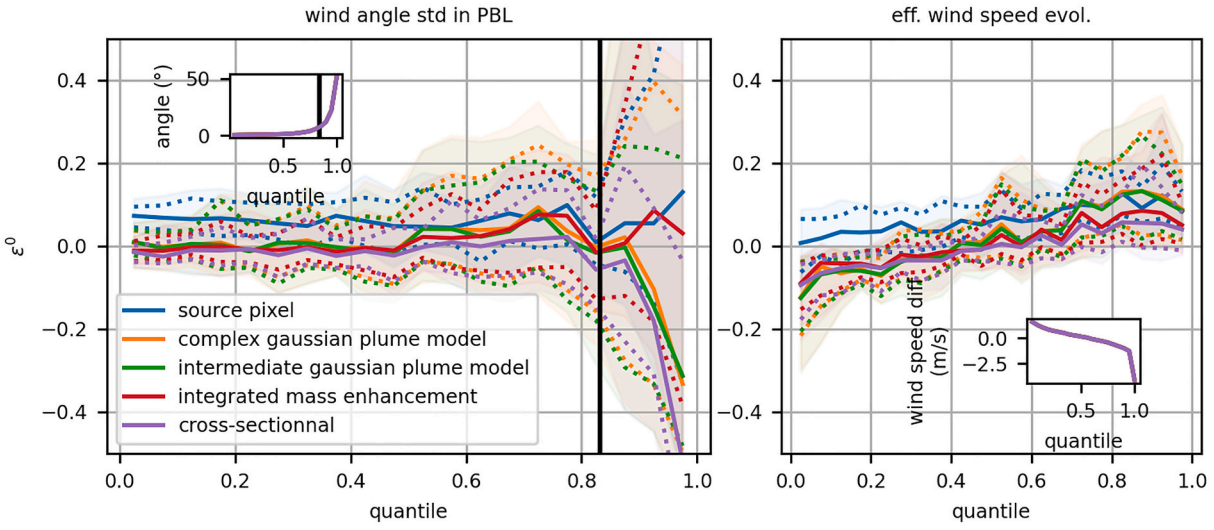

Fig. S4. Error distribution function of wind angle standard deviation in PBL before filtering (left panel) and function of the evolution of the effective wind speed in the previous hour after filtering (right panel). Results are shown for the different inversion methods using the '20 km–60 km' analysis zone for the Gaussian plume models and 'city-40 km' for IME and CS method. Black line on the right panel shows the threshold used for filtering the data.

After applying such a selection of the cases to be studied and for which to apply the emission computations, the accuracy of the results is strongly increased. The IQR of ε^0 decreases by 2–4% depending on the inversion method and the plume analysis zone. The biases of ε^0 are smaller than 2% (see Fig. S6), except for the SP method (6%).

However, such a selection does not cancel the high dependencies to the meteorological conditions (signal strength, effective wind speed, spatial variability of the wind direction, temporal variability of the wind speed). As an example, Fig. S4 illustrates the dependency to the temporal variability of the wind speed. The effective wind speed used by the emission calculation method is derived at the observation time without accounting for its temporal variations despite the plume is generally representative of several hours of emission and transport. Therefore, if the wind speed decreases in time, we tend to underestimate the wind speed that is representative of the overall plume, which leads to a positive bias in the distribution of ε^0. This effect increases with the distance of the analysis zone to the city center.

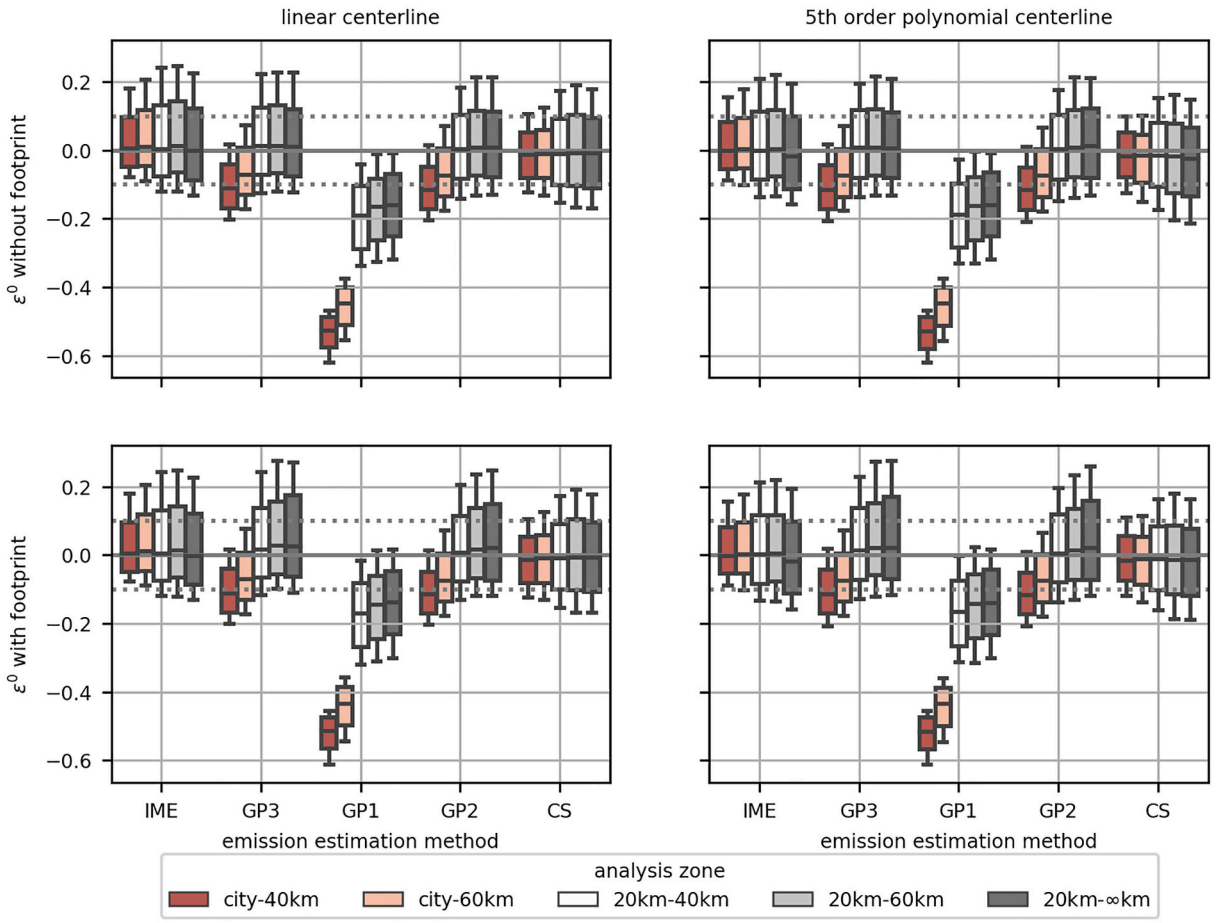

Fig. S5. Error distribution ε^0 in function of the tested parameters.

B.1.2.2. Influence of the centerline definition. The two centerline methods tested are, due to their definition, similar for the simple and intermediate Gaussian plume models and SP method.

The influence of the centerline definition on the GP3 and IME methods is the same as the one described for the CS method (see section B.1.1). When looking at the evolution of the error distribution ε^0 in function of the spatial distribution of the wind variability, the bias is smaller when using the 5th order polynomial centerline for cases corresponding to the third quartile of the wind direction variability than when using the linear centerline.

B.1.2.3. Influence of the analysis zone. The influence of the analysis zone definition was not studied for the SP method. For the IME and CS methods, the IQR of the distribution ε^0 increases with the distance of the analysis zone to the city center. Further of the city is the plume analysis zone, larger is the IQR of the distribution of ε^0. This is coherent with the results seen on Fig. S5 for the CS method. This effect seems to be present in a lesser way for the Gaussian plume inversions but with an evolution too small to be certain.

The results are different depending on the kind of method (mass-balance or Gaussian plume based) used for the emission calculation. For the IME methods, as seen on section B.1.1, the loss of mass occurring at the end of the plume (cropped by the image border) which begin at 60 km from the city results in a slight underestimation of the emissions when using analysis zones encompassing the part of the plume further than 60 km away of the city ('city-∞' and '20 km-∞') compared to the other analysis zones.

The Gaussian plume models are based on a fitting of the concentrations per pixel and thus are not influenced by the mass loss due to the cropping of the plume. However, the concentrations simulated by the Gaussian plume model above the city and downwind of the city center are obtained using the sum of the emissions on the whole targeted area. This is not the case in more realistic conditions as the source is not punctual (or linear) but has a 2D extension. This results in an overestimation of the the concentrations above the city and downwind of the city center by the Gaussian plume model and thus an underestimation of the emissions (bias inferior to −5%) during the inversions when using a analysis zone encompassing the part of the plume above the city.

B.1.2.4. Influence of the emission zone. For all the methods, the results are not affected by the application of the rescaling with the emission zones defined in section 3.8: 98% of the emission estimates show a difference of <5%.

B.1.2.5. Influence of the cross-section width. The results are slightly affected by the length used for the cross-sections. The distributions ε^0 show differences for biases and IQRs of <2%, for any combination of inversion methods, centerline definition and analysis zone.

B.1.2.6. Comparison of the Gaussin plume models. The simplest method yields very large biases (between −10 and − 50%) which can be attributed to

the high modelling errors associated to a model for which all parameters but the emissions are fixed without considering the observed plume. The stability parameter and the source radius fixed in this methods are generally far from those derived a priori (mean absolute difference of 7 km for the radius, and 70 for the stability parameter, which usually takes discrete values between 68 and 213).

The results obtained with the intermediate and complex Gaussian plume inversions are very similar. No differences can be seen at this stage between the two methods.

B.1.2.7. Summary of the options selection. We decided in the following to restrict to the results obtained with the 5th order polynomial centerline with the 'city-40 km', 'city-60 km', '20 km–40 km' and '20 km–60 km' analysis zone for the IME and CS methods and '20 km–40 km' and '20 km–60 km' for the GP inversions. The GP1 inversion is discarded as well as all the days for which the spatial variability of the wind direction in the PBL is superior to 7°. The distribution ε^0 in the selected configurations in shown on Fig. S6.

B.1.3. Analysis of ε_0^n

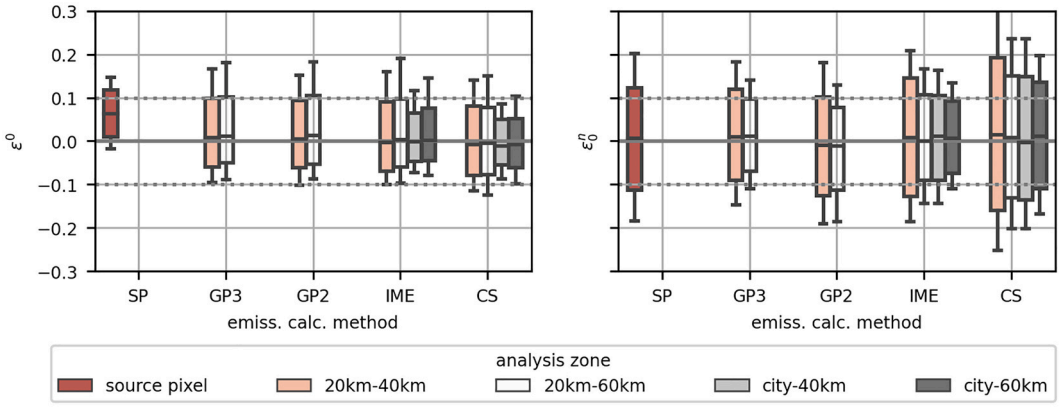

Fig. S6. Error distributions ε^0 and ε_0^n for the different analysis zones retained and inversion methods.

The error distribution ε_0^n is unbiased (absolute median value inferior to 2%) and with a relatively small IQR (between 17% and 27%, see Fig. S6), except for the CS method (between 25 and 35%).

For a given image, taking a larger analysis zone generally increases the number of points used for the emission calculation and thus lessen the impact of the measurement noise on the estimation. Therefore, Fig. S6 shows that larger is the plume analysis zone, lower is the IQR of the ε_0^n. When considering the combination of ε^0 and ε_0^n the "optimal" analysis zone appear to be a compromise between the size of the zone and its distance to the city center.

The amplitude of ε_0^n is mainly driven by the wind speed (larger wind speed yielding larger ε_0^n), since the wind speed directly defines the amplitude of the plume and thus the signal to noise ratio (defined as the mean signal XCO_2 for Paris core urban area divided by the difference between the values of the first and last deciles of the background -including noise- signal) exploited by the emission computation. This positive sensitivity of the amplitude of ε_0^n to the wind speed balances the negative sensitivity of the amplitude of ε^0 to the mean effective wind speed (see section B.1.2). However, the combination of ε^0 and ε_0^n keeps on having a much larger amplitude for cases with a spatial variability of the wind direction above the threshold identified in 4.1 compared to cases for which the spatial variabilit of the wind direction is below this threshold. This implicitly implies a tendency to retain large wind speeds when applying the threshold, due to the correlation of the two (see section B.1.2). Therefore, the selection applied on the cases based on this threshold remains relevant when accounting for ε_0^n.

B.2. Evaluation of the wind estimation

In this section, the performance of the wind methods described on section 3.6 are analyzed based on the dependencies of the error distribution ε_0^w (section B.2.1) and ε_n^w (section B.2.2) to those methods and their parameters. The methods are compared and the some configurations set aside.

B.2.1. Analysis of ε_0^w

Fig. S7 shows the error distribution ε_0^w for the different wind estimation methods. The distribution of the error is only slightly influenced by the inversion method for a given analysis zone.

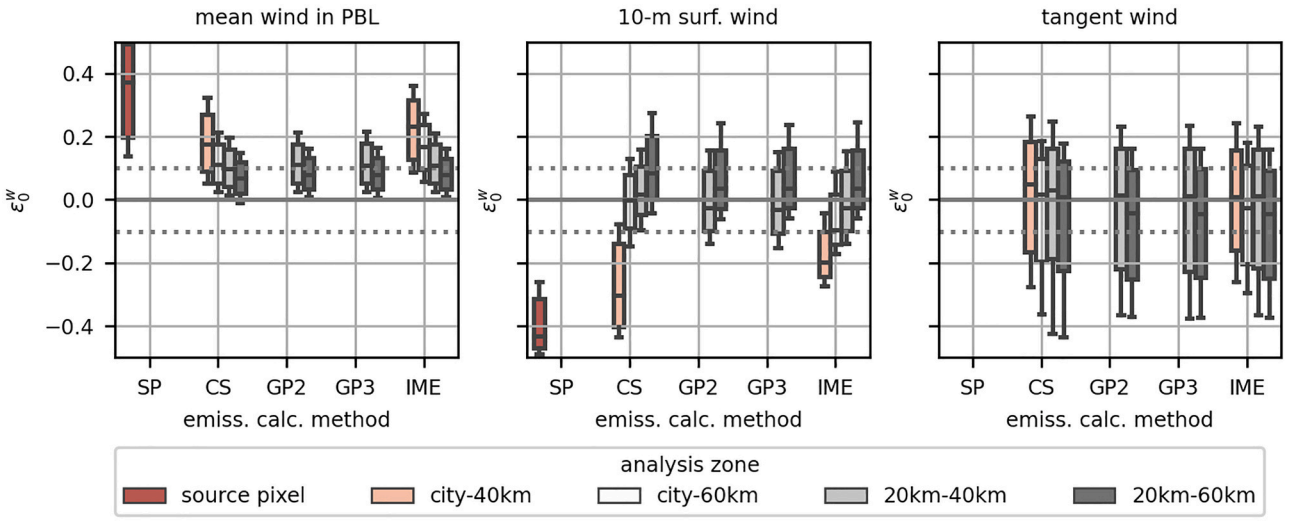

Fig. S7. Distribution of ε_0^w for the different wind estimation methods function of the inversion methods and the analysis zone.

ε_0^w bears much larger biases (respectively −43% to +8% and + 37% to 7%) when using the surface and mean wind estimation methods but a narrower IQR (respectively 14% to 26% and 10% to 19% with the exception when using the SP method at 29%) than when using the tangent wind estimation method (with which the bias is smaller than 5% but the IQR is larger than 31%). The small IQR of the first two methods indicates a good correlation between the effective wind and the estimated wind.

The amplitude of ε_0^w when using the surface wind (middle panel) and the mean wind in the PBL (left panel) to estimate the effective wind depends on the analysis zone, both in term of IQR and bias. When the analysis zone is far from the source, the corresponding section of the CO_2 plume is well mixed in the PBL and the mean wind method gives an estimation with low bias and IQR. The distribution of ε_0^w when using the tangent wind estimation method (right panel) is not really influenced by the general definition of the analysis zone. We thus choose to select the method of wind estimation as a function of the analysis zone: the tangent wind is used with the 'city-40 km' and 'city-60 km' analysis zones and the mean wind in PBL with the '20 km–40 km' and '20 km–60 km' analysis zone. This choice applies in the following of this section and of this study.

The IQR of ε_0^w is influenced by the wind direction variability when using the mean wind estimation method and even more the surface wind estimation method (not shown). As the spatial variability of the wind direction increases, the plume complexity increases and thus the difficulty to find a wind that is representative of the plume increases.

B.2.2. Analysis of ε_n^w

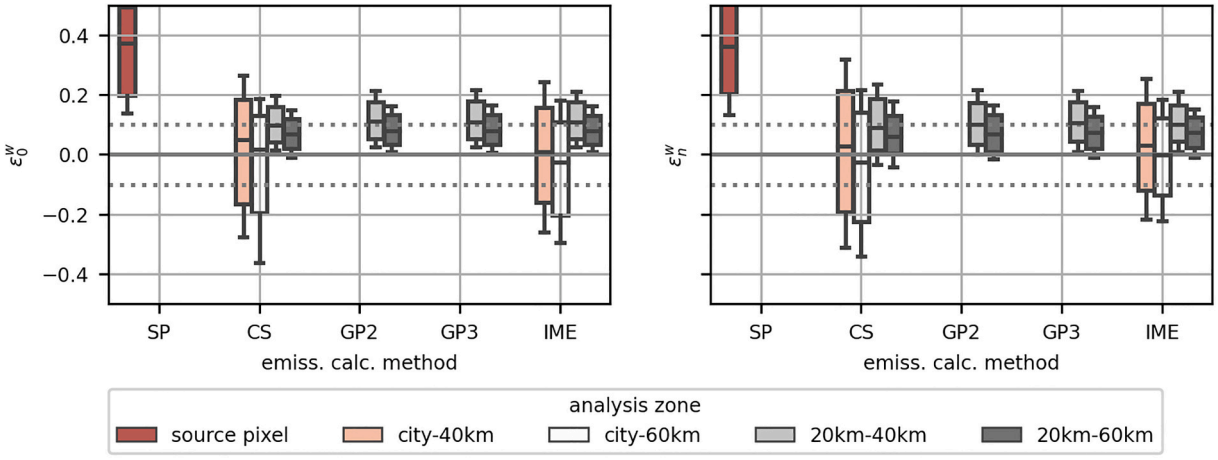

Fig. S8. Error distributions ε_0^w and ε_n^w for the different analysis zones and wind methods retained in function of the inversion method.

ε_n^w is similar to the error distribution ε_0^w in term of sensibility to the inversion method, analysis zone and spatial variability of the wind direction. The selection of the wind method in function of the analysis zone described in section B.2.1 is thus used in the following. Fig. S8 shows the error distribution in function of the analysis zone and inversion methods for the wind methods retained. For the analysis zone encompassing the city (i.e. when using the tangent wind method) when using the Integratd Mass Enhancemet method, the IQR of the distribution ε_n^w is slightly smaller than the IQR of ε_0^w, which may indicate a slight overfiting of the centerline close to the city center, overfitting which disappear when the noise is added. However the relation between the wind estimation method and the centerline is complex and the hypothesis is thus difficult to assess.

B.3. Evaluation of the plume definition methods with perfectly known background: analysis of ε_n^p

In this section, the performance of the plume definition methods and emission zone definitions are analyzed via the error distribution ε_n^p. This section verify their performances in the absence of background and let us make a small narrowing of the options at the end.

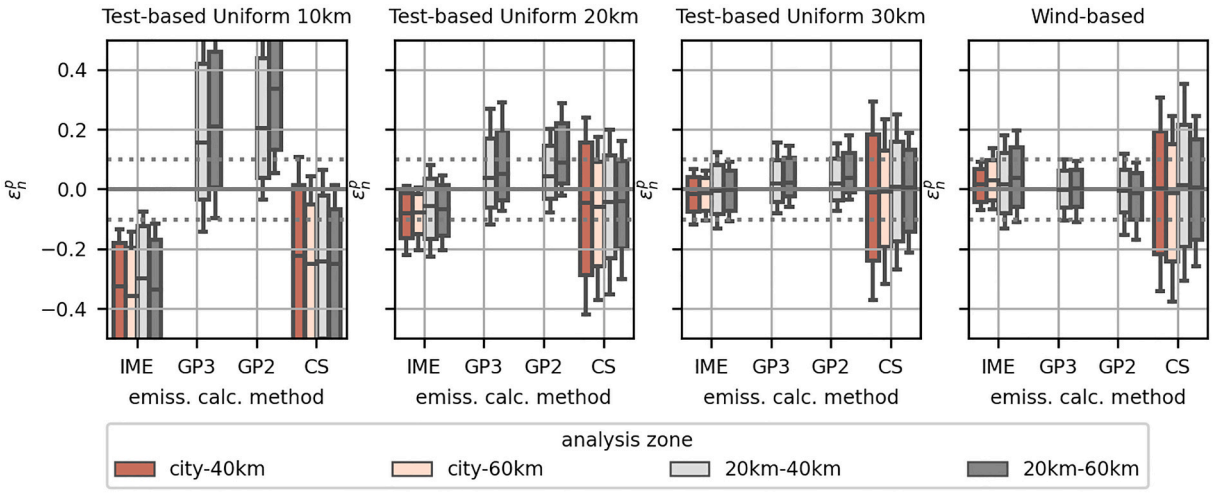

Fig. S9. Distribution of ε_n^p in function of the inversion methods and analysis zone for the selected plume definition methods. The error shows the results whith no rescaling.

The two kinds of methods, the ones based on a statistical test on the smoothed XCO_2 data and the one based on the wind direction, show acceptable results when well parameterized, with bias of the error distribution ε_n^p inferior to 10% and IQR inferior to 35% (see Fig. S9). The IQR is again higher when using the CS method.

In Fig. S10 the skill of the plume definition is quantified in terms of the fraction of the number of pixels of the real plume that as been detected on (i) the number of pixels in the real plume (denoted detection precision) and (ii) the number of pixels in the detected plume (denoted detection level).

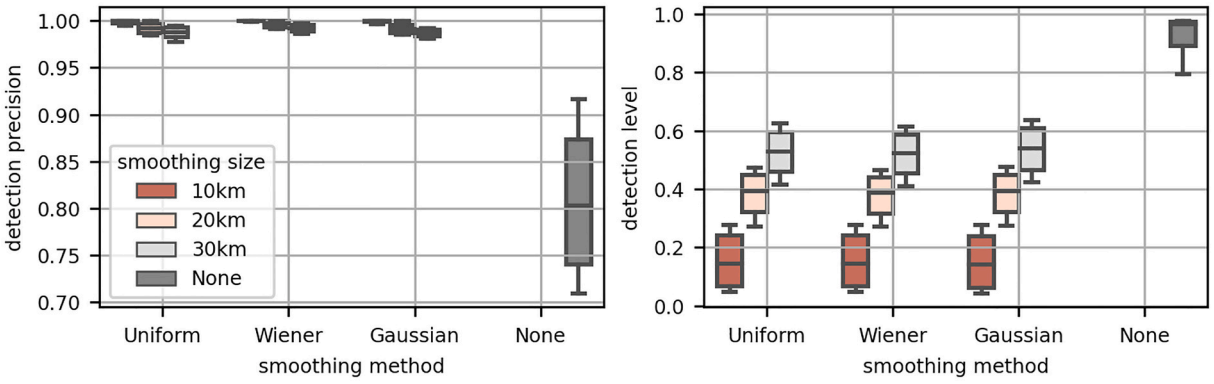

Fig. S10. Detection level (lower panel) and precision (upper panel) in function of the plume definition methods. The label None on the x-axis corresponds to the wind-based method.

The statistical test of the first kind of plume definition method is made for the same kind of distribution as the one of the observation uncertainty. Those methods therefore show good detection precision: all the plume definitions with this kind of method have a detection level above 0.9, which means that >90% of the pixels that have been labeled as part of the plume really belong to the plume for every parametrization. As the smoothing size increases, more non -plume pixels are contaminated by plume pixels during the smoothing and therefore the detection precision decreases. With the wind-based method, the detection precision is smaller (median of 0.8) as it does not rely on the XCO_2 field.

The test-based methods leave aside the plume pixels with a small signal. Therefore the detection levels are small and decrease with the smoothing size. Even with a 30 km smoothing size, 75% of the plume definitions show detection levels below 0.6, which means that 40% of the plume has not been detected. The wind-based method shows better detection level than the test-based methods, with 84% of the plume definition with detection level above 0.8.

For the test-based methods, the plume definition and detection level show no sensitivity to the smoothing method. Therefore we focus hereafter on the results obtained with the Uniform smoothing method.

Fig. S9 shows the error distribution ε_n^p for the different plume definition methods. A low detection level indicates a high level of plume pixels non detected and thus leads to a negative bias of the error distribution ε_n^p for CS and IME methods (bias inferior to −22% with the 10 km smoothing size). The low detection levels affect also the Gaussian inversions, with a positive bias on the error distribution ε_n^p (bias superior to 15% with the 10 km smoothing size). Therefore, the absolute bias of the error distribution decreases with the smoothing size of the test-based methods. Of note is that a median detection level of only 0.4 leads to a absolute bias of the error distribution ε_n^p for CS and IME methods inferior to 10%.

The application of the emission zone for the IME and CS methods reduces the bias for the small smoothing sizes (bias inferior to 5% for the 20 km smoothing size for the IME and CS methods), but without reaching the level of bias of the 30 km smoothing size. For the Gaussian plume inversions, the IQR of the error distribution is stable when applying the emission zone for the 10 km smoothing size (range from 40% to 46% with no rescaling and

42% to 45% with rescaling) and the 20 km smoothing size (range from 18% to 23% with no rescaling and 19% to 26% with rescaling). For the 30 km smoothing size, the cross-section of the plume are bigger than the city radius and thus all the Paris core urban area is within the emission zone in most cases. As there is no background, no emissions outside of the Paris core urban area are put in the emission zone. Thus the emission zone is strictly equivalent to the Paris core urban area in most cases: 18% to 84% of the cases (71% to 84% when we exclude results obtained with the CS method) show a difference inferior to 5% between this two reference emissions (13% to 86% with a 20 km smoothing size, 25% to 86% when excluding CS results). The emission zone definition are thus not very relevant to improve the performance of the plume definition methods when analyzing the error distribution ϵ_n^p.

The high detection level of the wind direction based method means that a large fraction of the plume is caught. As the false-positive distribution should have a mean value of 0, there impact are small on the inversion methods. The error distribution of ϵ_n^p has thus a small bias (between −1% and 4%) and IQR (between 11% and 41%) when using the plume definition method based on the wind direction.

The IQR of ϵ_n^p, as the IQR of ϵ_0^n, is driven by the ratio between the strength of the XCO_2 signal and the measurement noise (the "signal-to-noise-ratio" of the plume definition). In the case of the test-based plume definition methods, the bias of ϵ_n^p is also sensitive to the signal to noise ratio: the detection level increases with the signal-to-noise-ratio, which result in a decrease of the bias of ϵ_n^p with the signal-to-noise-ratio.

B.4. Evaluation of the background estimation methods with perfectly known plume

In this section, the performance of the background estimation methods described on section 3.3 are analyzed based on the dependencies of the error distribution ϵ_0^b (section B.4.1) and ϵ_n^b (section B.4.2) to those methods and their parameters. The methods are compared and the some configurations set aside.

B.4.1. Analysis of ϵ_0^b

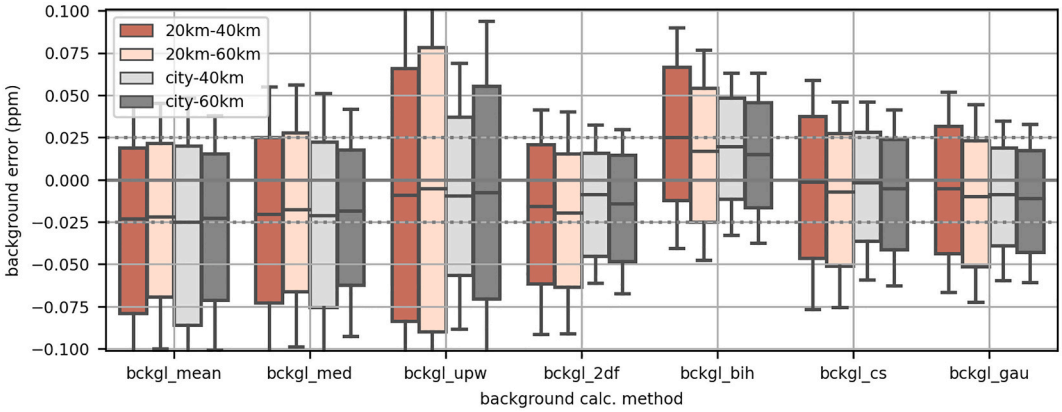

Fig. S11. Distribution of the background error in function of the background estimation method for the different plume analysis zones.

The mean error of the calculated background in the analysis zone of interest is calculated for each image and background calculation methods. We first study the distribution of this mean error (denoted background error in the following, see Fig. S11) in function of the analysis zone and background calculation methods to make a preselection of the background calculation methods.

For the analysis zone of the SP method, two background estimation methods stands out with a relatively small bias of the background error (absolute value of the median inferior to 0.01 ppm): 'bckgl_mean' and 'bckgl_gauss'. For the analysis zones used by the other emission calculation methods, the bias and the IQR of the distribution of the background error are low (bias inferior to 0.01 ppm and IQR inferior to 0.09 ppm for all the analysis zone) when using 'bckgl_cs' and bckgl_gau' methods. The method based on biharmonic equation ('bckgl_bih'), albeit having a similar IQR, gives a median bias for the background error around 0.025 ppm, which results in a median bias around 25% for the distribution of ϵ_0^b. We thus decide to focus on the 'bckgl_mean' and 'bckgl_gauss' methods for the source pixel analysis zone and on the 'bckgl_cs' and 'bckgl_gau' methods for the other plume analysis zones.

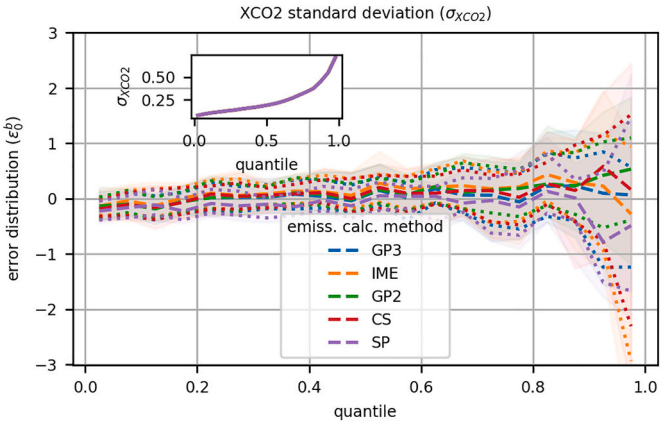

Fig. S12. Illustration with the 'bckgl_gau' method of the evolution of the distribution ϵ_0^b in function of the standard deviation of the XCO_2 signal in the image for the different inversion methods.

The error distribution ϵ_0^b shows no sensitivity to the analysis zone (not shown), therefore the following results are presented using the 'city-40 km' analysis zone for CS and IME methods and '20 km–60 km' for the Gaussian inversions, but the conclusions can be extended to the other plume analysis zone.

The complexity of the background, when too important, can not be modeled by the methods used for the background calculation. Therefore the IQR of the distribution ϵ_0^b increases with the standard deviation of the XCO_2 field in the image (see Fig. S12) and this standard deviation is a good indicator of the expected accuracy of the emission calculation.

When the plume is occupying >40% of the image, the background methods faces difficulties to resolve the center of the plume. When the plume is unknown, the designs of our plume definition method do not allow for the plume detected to reach such size. Thus this effect is not a problem in our study but attention should be paid to this point when the city is occupying a bigger part of the image.

B.4.2. Analysis of ϵ_n^b

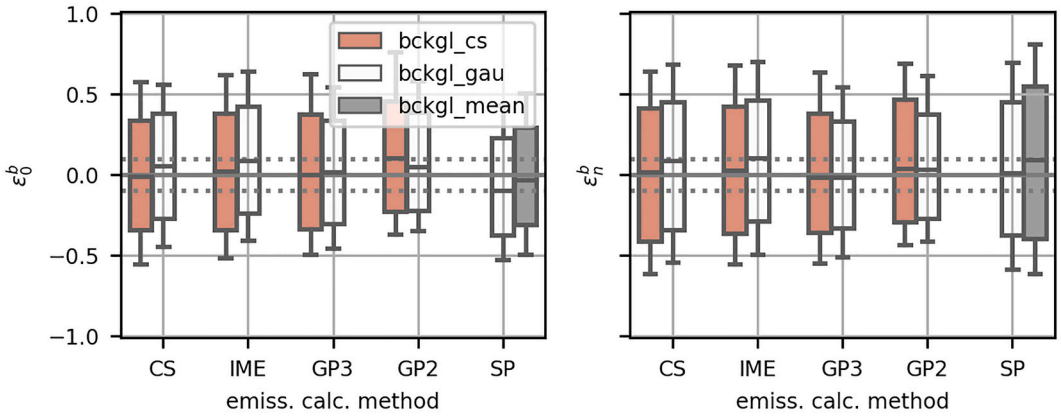

Fig. S13. Distribution of ϵ_0^b and ϵ_n^b in function of the background calculation methods for the different inversion methods.

When the measurement noise is added, the background calculation methods show similar results than in the previous section. The distribution ϵ_n^b is thus similar to ϵ_0^b (see Fig. S13). The sensitivity to the standard deviation of the XCO_2 field in the image and the plume size are found to be the same.

B.5. Combined effect of the plume and background methods

This section only concern the IME and CS methods and GP inversions as the SP method does not need a detection of the plume limits.

Only the background calculation methods selected in section B.4 and the plume definition methods selected in B.3 are studied. The performance of the plume definition and background calculation methods are studied regarding their results in terms of background error, detection level and detection precision (section B.5.1) and by analyzing the error distributions ϵ_b^p (section B.5.2) and ϵ_{nb}^p (section B.5.3). The range of options is narrowed in each subsection.

B.5.1. First evaluation of the methods performance

The simulation are made with a unknown plume and background and a 0.7 ppm noise. A first evaluation is made of the combination of the retained background calculation methods (see section B.4) and the plume definition methods in terms of background error in the analysis zones (see section B.3), detection sensitivity, detection precision and number of plume successfully detected.

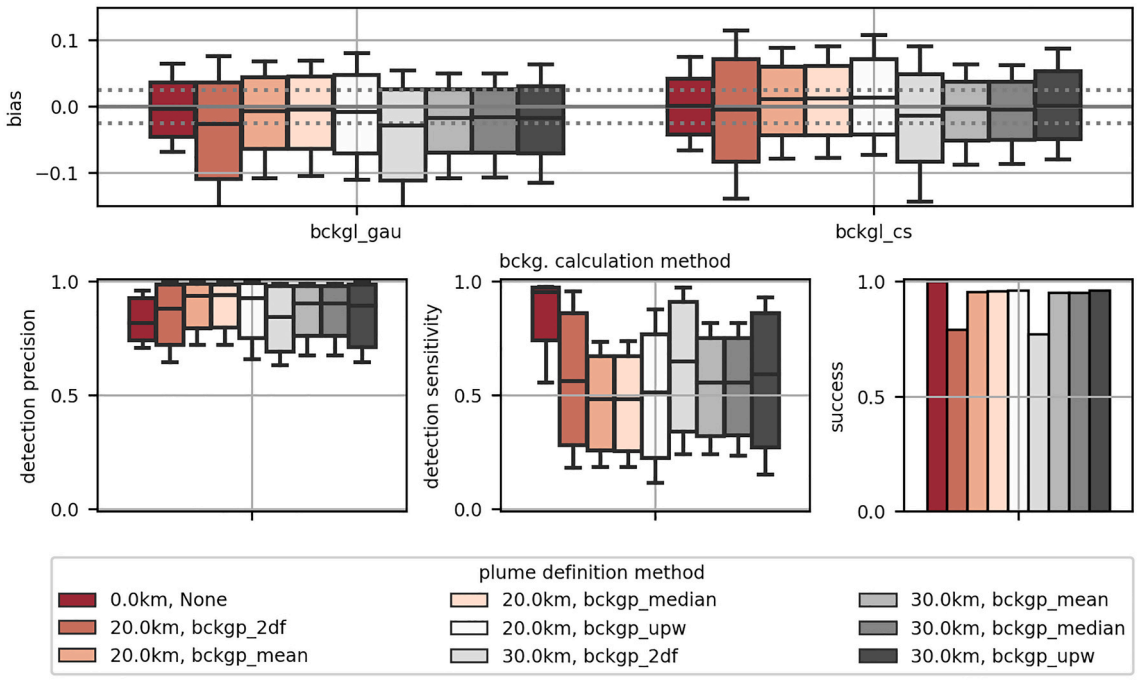

Fig. S14. Results of the different plume definition and background calculation methods in terms of background error, detection sensitivity, detection precision and number of plume successfully detected. The results are grouped by a priori background calculation method. Only the parametrizations of the test-based method using a uniform filter are shown.

The for indicators show no sensitivity to the analysis zone (not shown), thus we focus on the 'city-60 km' analysis zone hereafter. Fig. S14 shows an illustration of the results for the selected plume analysis zone. We first focus on the tuning of the plume definition method adapted from Kuhlmann et al. (2019) (Fig. S14) where the method for the a priori calculation of the background, the smoothing method and smoothing size have to be chosen. For a given a priori background calculation and smoothing size, the results given by the different smoothing method are very close: the pearson correlation between the smoothing methods for the detection sensitivity and precision are superior to 0.97. The for indicators show low sensitivity to the smoothing size: a 20 km smoothing size will give a slightly bigger background, a better detection precision but a lower detection sensitivity. This difference is more or less marked depending on the a priori background calculation method used.

Concerning the method for the a priori background calculation, the one based on a planar fit of the XCO_2 data (bckgp_2df) shows a significant IQR (between 0.13 and 0.16 ppm) compared to the other methods (between 0.09 and 0.12). This method gives also low detection precision compared to the other a priori background calculation methods. The methods based on the median and the mean of the XCO_2 data (resp. bckgp_mean and bckgp_med) give very similar results (correlation over 0.97 for the detection precision, detection sensitivity and background error). Therefore we choose to focus on the methods bckgp_mean and bckgp_upw. The bckgp_mean method has a smaller background error than the bckgp_upw method and shows a slightly better detection precision but a smaller detection sensitivity. We thus choose to keep in the following only two version of the plume definition method adapted from Kuhlmann et al. (2020): (i) an a priori calculation of the background with the bckgp_upw method associated to a 20 km smoothing size with the Uniform smoothing method and (ii) an a priori calculation of the background with the bckgp_mean method associated to a 20 km smoothing size with the Uniform smoothing method. Both background calculation methods tested (bckgl_cs and bckgl_gau) are kept.

The results given by the wind-based method are similar to the test-based methods retained in term of background error: the IQR of the background error distribution are around 0.08 ppm and the bias is inferior to 0.005 ppm for all of them. The detection precision and sensitivity are different with a much narrower IQR (detection precision: 0.19 for the wind based, between 0.19 and 0.28 for the test-based; detection sensitivity: 0.23 for the wind based, between 0.41 and 0.59 for the test-based). As in the case of ε_n^p, for the wind-based method the median detection precision is slightly smaller (0.82 for the wind-based, 0.89 and 0.94 for the test-based) but the median detection sensitivity is far greater (0.94) than when the test-based methods are used (0.48 and 0.61).

B.5.2. Analysis of ε_b^p

The simulations are performed with an unknown background, unknown plume and no measurement noise in the configurations selected in section B.5.1. The distribution of ε_b^p shows a high sensitivity to the configuration parameters (plume analysis zone, background calculation and plume definition method).

The IQR of the distribution ε_b^p increases with the distance of the analysis zone to the city center. Close to the core urban area, the targeted XCO_2 signal do not have time to diffuse and is thus strong and directly downwind of the core urban area. Thus the plume definition methods may perform better on analysis zone close to the core urban area and explain this sensitivity not seen in the previous section. The results described in the rest of the subsection being independent of the plume analysis zone, we present the results with the 'city-40.0 km' analysis zone for the CS and IME methods and '20.0–40.0 km' analysis zone for the GP inversions.

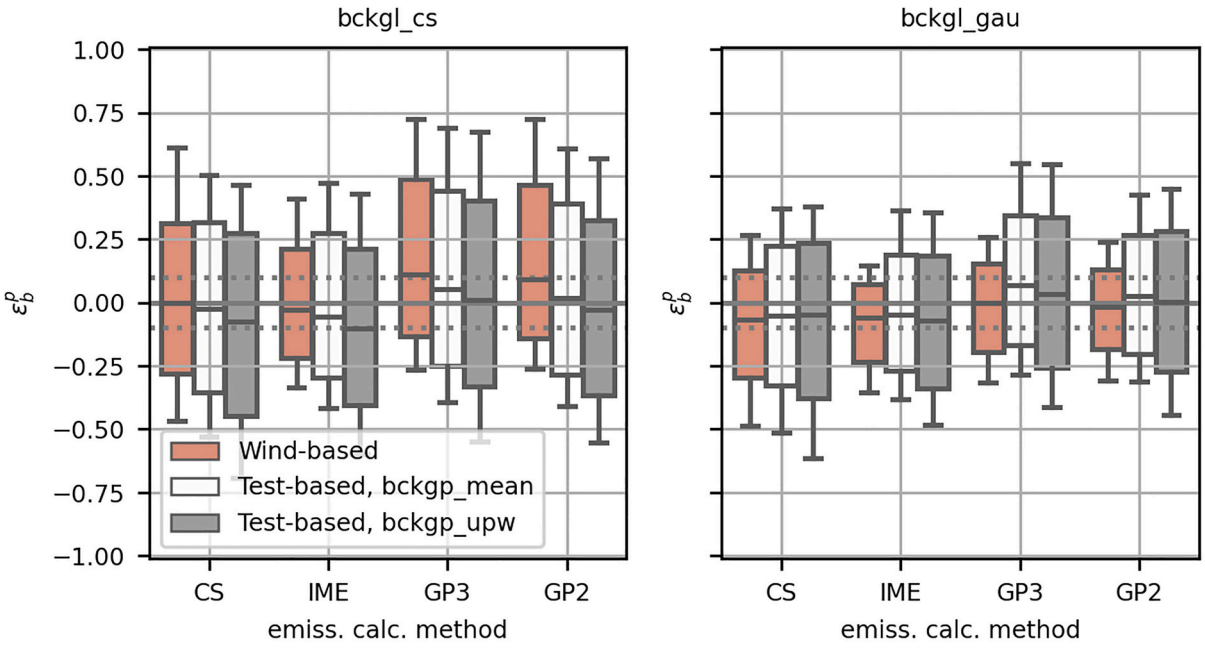

Fig. S15. Distribution of ε_b^p in function of the emission calculation for the different plume definition methods when using the 'bckgl_gau' (left panel) and 'bckgl_cs' (right panel) background calculation methods. The results are shown when using a uniform smoothing at 20 km for the test-based methods.

Fig. S15 show the distribution of ε_b^p, in function of the inversion methods and plume definition methods for the two background calculation methods retained. The results outlined in the previous section are confirmed here. The statistical based methods for plume definition tends to have a high number of false positive in the detected plume, which results in a lower detection level compared to the one obtained with the wind based method. This results in a bigger IQR in the distribution ε_b^p when using the statistical-based methods rather than the wind-based one for the plume definition. The use of the emission zone for the CS method reduce the IQR of the error distribution when using the test based plume definition methods, but not sufficiently for this methods to be interesting compared to the wind-based method.

The slightly bigger IQR of the background error seen in Fig. S14 when using the 'bckgl_cs' background calculation method rather than the 'bckgl_gau' one is enhanced in the distribution ε_b^p. Therefore, the best configuration seems, at this stage, the plume definition method based on the wind direction and the background calculation method based on Gaussian function. The application of the rescaling by the emission zone does not sufficiently improve the results of the test-based methods to be competitive with the wind-based methods.

The IQR of the distribution ε_b^p, as the IQRs of the distributions ε_n^p, ε_0^b and ε_n^b, is sensitive to the signal-to-noise ratio and thus increases with the standard deviation of the XCO_2 signal in the image.

B.5.3. Analysis of ε_{nb}^p and narrowing of the range of options for the background calculation and plume definition

The simulations are performed with an unknown background, unknown plume and 0.7 ppm measurement noise. The results found in the previous section in term of performance of the plume definition and background calculation methods are the same here. Therefore we focus on the results given by the plume definition method based on the wind direction and the background calculation method 'bckgl_gau'. A sensitivity to the analysis zone similar than for ε_b^p (see section B.5.2) is visible for ε_{nb}^p, except for the CS method. The IQR of the distribution ε_{nb}^p -as the distributions ε_n^p, ε_0^b and ε_n^b- decreases with the signal to noise ratio. Furthermore, this IQR slightly increases with the distance of the analysis zone to the city.

In the following, only the plume definition method based on the wind direction with the 'bckgl_gau' background calculation method are kept.

B.6. Analysis of ε_{nbp}^w

The distribution of ε_{nbp}^w shows -as ε_n^w and ε_0^w- a more important IQR when the tangent wind is used (32% to 52% vs 13% to 21% when the mean wind is used), which correspond to the analysis zones encompassing the city. The uncertainty in the estimation of the XCO_2 signal from the city, due to uncertainties in the plume limits and in the calculated background, impacts the estimation of the wind. Thus the IQR of ε_{nbp}^w (13% to 52%) is more important than the IQR of ε_n^w (10% to 47%). The bias is of the same order of magnitude (<10%).

When the signal to noise ratio is high, the weighting coefficient used to calculated the mean wind in the analysis zone are less accurate. Thus the IQR of the distribution increases with the signal to noise ratio and the standard deviation of the XCO_2 signal in the image.

References

Ahmadov, R., Gerbig, C., Kretschmer, R., Koerner, S., Neininger, B., Dolman, A.J., Sarrat, C., 2007. Mesoscale covariance of transport and co_2 fluxes: evidence from observations and simulations using the wrf-vprm coupled atmosphere-biosphere model. J. Geophys. Res. Atmos. 112, 1–14. https://doi.org/10.1029/2007JD008552. ISSN 01480227.

Ahmadov, R., Gerbig, C., Kretschmer, R., Körner, S., Rödenbeck, C., Bousquet, P., Ramonet, M., 2009. Comparing high resolution wrf-vprm simulations and two global co 2 transport models with coastal tower measurements of co2. Biogeosciences 6, 807–817. https://doi.org/10.5194/bg-6-807-2009. ISSN 17264189.

Bréon, F.-M., Broquet, G., Puygrenier, V., Chevallier, F., Xueref-Remy, I., Ramonet, M., Dieudonné, E., Lopez, M., Schmidt, M., Perrussel, O., Ciais, P., 2015. An attempt at estimating Paris area co_2 emissions from atmospheric concentration measurements. Atmos. Chem. Phys. 15, 1707–1724. https://doi.org/10.5194/acp-15-1707-2015. ISSN 16807324.

Broquet, G., Bréon, F.-M., Renault, E., Buchwitz, M., Reuter, M., Bovensmann, H., Chevallier, F., Wu, L., Ciais, P., 2018. The potential of satellite spectro-imagery for monitoring co_2 emissions from large cities. Atmos. Meas. Tech. 11, 681–708. https://doi.org/10.5194/amt-11-681-2018. ISSN 18678548.

Buchwitz, M., Schneising, O., Reuter, M., Heymann, J., Krautwurst, S., Bovensmann, H., Burrows, J.P., Boesch, H., Parker, R.J., Somkuti, P., Detmers, R.G., Hasekamp, O.P., Aben, I., Butz, A., Frankenberg, C., Turner, A.J., 2017. Satellite-derived methane hotspot emission estimates using a fast data-driven method. Atmos. Chem. Phys. 17, 5751–5774. https://doi.org/10.5194/acp-17-5751-2017. ISSN 16807324.

Chevallier, F., Zheng, B., Broquet, G., Ciais, P., Liu, Z., Davis, S.J., Deng, Z., Wang, Y., Bréon, F.-M., O'Dell, C.W., 2020. Local anomalies in the column-averaged dry air mole fractions of carbon dioxide across the globe during the first months of the coronavirus recession. Geophys. Res. Lett. 47 https://doi.org/10.1029/2020GL090244. ISSN 19448007.

Chevallier, F., Broquet, G., Zheng, B., Ciais, P., Eldering, A., 2022. Large co 2 emitters as seen from satellite: comparison to a gridded global emission inventory. Geophys. Res. Lett. https://doi.org/10.1029/2021gl097540. ISSN 0094-8276.

Ciais, P., Crisp, D., van der Gon, H.D., Engelen, R., Janssens-Maenhout, G., Heimann, M., Rayner, P., Scholze, M., 2015. Towards a European Operational Observing System to Monitor Fossil Co_2 Emissions.

Ciais, P., Wang, Y., Andrew, R., Bréon, F.-M., Chevallier, F., Broquet, G., Nabuurs, G.J., Peters, G., Mcgrath, M., Meng, W., Zheng, B., Tao, S., 2020. Biofuel burning and human respiration bias on satellite estimates of fossil fuel co2emissions. Environ. Res. Lett. 15 https://doi.org/10.1088/1748-9326/ab7835. ISSN 17489326.

Deng, A., Lauvaux, T., Davis, K.J., Gaudet, B.J., Miles, N., Richardson, S.J., Wu, K., Sarmiento, D.P., Hardesty, R.M., Bonin, T.A., Brewer, W.A., Gurney, K.R., 2017. Toward reduced transport errors in a high resolution urban co_2 inversion system. Elementa 5. https://doi.org/10.1525/elementa.133. ISSN 23251026.

Díaz-Isaac, L.I., Lauvaux, T., Davis, K.J., 2018. Impact of physical parameterizations and initial conditions on simulated atmospheric transport and co_2 mole fractions in the us Midwest. Atmos. Chem. Phys. 18, 14813–14835. https://doi.org/10.5194/acp-18-14813-2018. ISSN 16807324.

Dumont Le Brazidec, J., Vanderbecken, P., Farchi, A., Broquet, G., Kuhlmann, G., Bocquet, M., 2023. Deep learning applied to CO 2 power plant emissions quantification using simulated satellite images. https://doi.org/10.5194/gmd-2023-142.

Eldering, A., O'Dell, C.W., Wennberg, P.O., Crisp, D., Gunson, M.R., Viatte, C., Avis, C., Braverman, A., Castano, R., Chang, A., Chapsky, L., Cheng, C., Connor, B., Dang, L., Doran, G., Fisher, B., Frankenberg, C., Fu, D., Granat, R., Hobbs, J., Lee, R.A., Mandrake, L., McDuffie, J., Miller, C.E., Myers, V., Natraj, V., O'Brien, D., Osterman, G.B., Oyafuso, F., Payne, V.H., Pollock, H.R., Polonsky, I., Roehl, C.M., Rosenberg, R., Schwandner, F., Smyth, M., Tang, V., Taylor, T.E., To, C., Wunch, D., Yoshimizu, J., 2017. The orbiting carbon observatory-2: First 18 months of science data products. Atmos. Measure. Tech. 10, 549–563. https://doi.org/10.5194/amt-10-549-2017. ISSN 18678548.

Eldering, A., Taylor, T.E., O'Dell, C.W., Pavlick, R., 2019. The Oco-3 mission: measurement objectives and expected performance based on 1 year of simulated data. Atmos. Meas. Tech. 12, 2341–2370. https://doi.org/10.5194/amt-12-2341-2019. ISSN 18678548.

Feng, S., Lauvaux, T., Newman, S., Rao, P., Ahmadov, R., Deng, A., Díaz-Isaac, L.I., Duren, R.M., Fischer, M.L., Gerbig, C., Gurney, K.R., Huang, J., Jeong, S., Li, Z., Miller, C.E., O'Keeffe, D., Patarasuk, R., Sander, S.P., Song, Y., Wong, K.W., Yung, Y. L., 2016. Los Angeles megacity: a high-resolution land-atmosphere modelling system for urban co_2 emissions. Atmos. Chem. Phys. 16, 9019–9045. https://doi.org/10.5194/acp-16-9019-2016. ISSN 16807324.

Frankenberg, C., Thorpe, A.K., Thompson, D.R., Hulley, G., Kort, E.A., Vance, N., Borchardt, J., Krings, T., Gerilowski, K., Sweeney, C., Conley, S., Bue, B.D., Aubrey, A.D., Hook, S., Green, R.O., 2016. Airborne methane remote measurements reveal heavytail flux distribution in four corners region. Proc. Natl. Acad. Sci. U. S. A. 113, 9734–9739. https://doi.org/10.1073/pnas.1605617113. ISSN 10916490.

Gerber, F., Jong, R.D., Schaepman, M.E., Schaepman-Strub, G., Furrer, R., 2018. Predicting missing values in spatio-temporal remote sensing data. IEEE Trans. Geosci. Remote Sens. 56, 2841–2853. https://doi.org/10.1109/TGRS.2017.2785240. ISSN 01962892.

Gurney, K.R., Liang, J., Roest, G., Song, Y., Mueller, K., Lauvaux, T., 2021. Under-reporting of greenhouse gas emissions in u.s. cities. Nat. Commun. 12, 1–7. https://doi.org/10.1038/s41467-020-20871-0. ISSN 20411723. URL doi:10.1038/s41467-020-20871-0.

Inness, A., Ades, M., Agustí-Panareda, A., Barr, J., Benedictow, A., Blechschmidt, A.M., Dominguez, J.J., Engelen, R., Eskes, H.J., Flemming, J., Huijnen, V., Jones, L., Kipling, Z., Massart, S., Parrington, M., Peuch, V.H., Razinger, M., Remy, S., Schulz, M., Suttie, M., 2019. The cams reanalysis of atmospheric composition. Atmos. Chem. Phys. 19, 3515–3556. https://doi.org/10.5194/acp-19-3515-2019. ISSN 16807324.

Janjic, Z.I., 1990. The step-moutain coordinate: physical package. Mon. Weather Rev. 118, 1429–1443 doi:10.1175/1520-0493(1990)118<1429:TSMCPP>2.0.CO;2.

Janjic, Z.I., 1994. The step-mountain eta coordinate model: further developments of the convection, viscous sublayer, and turbulence closure schemes. Mon. Weather Rev. 927–945 doi:10.1175/1520-0493(1994)122<0927:TSMECM>2.0.CO;2.

Janssens-Maenhout, G., Pinty, B., Dowell, M., Zunker, H., Andersson, E., Balsamo, G., Bézy, J.L., Brunhes, T., Bösch, H., Bojkov, B., Brunner, D., Buchwitz, M., Crisp, D., Ciais, P., Counet, P., Dee, D., van der Gon, H.D., Dolman, H., Drinkwater, M.R., Dubovik, O., Engelen, R., Fehr, T., Fernandez, V., Heimann, M., Holmlund, K., Houweling, S., Husband, R., Juvyns, O., Kentarchos, A., Landgraf, J., Lang, R., Löscher, A., Marshall, J., Meijer, Y., Nakajima, M., Palmer, P.I., Peylin, P., Rayner, P., Scholze, M., Sierk, B., Tamminen, J., Veefkind, P., 2020. Toward an operational anthropogenic co_2 emissions monitoring and verification support capacity. Bull. Am. Meteorol. Soc. 101, E1439–E1451. ISSN 00030007. doi:10.1175/BAMS-D-19-0017.1.

Kort, E.A., Angevine, W.M., Duren, R.M., Miller, C.E., 2013. Surface observations for monitoring urban fossil fuel co_2 emissions: minimum site location requirements for the los Angeles megacity. J. Geophys. Res. Atmos. 118, 1577–1584. https://doi.org/10.1002/jgrd.50135. ISSN 21698996.

Krings, T., Gerilowski, K., Buchwitz, M., Reuter, M., Tretner, A., Erzinger, J., Heinze, D., Pflüger, U., Burrows, J.P., Bovensmann, H., 2011. Mamap - a new spectrometer system for column-averaged methane and carbon dioxide observations from aircraft: retrieval algorithm and first inversions for point source emission rates. Atmos. Meas. Tech. 4, 1735–1758. https://doi.org/10.5194/amt-4-1735-2011. ISSN 18671381.

Kuhlmann, G., Broquet, G., Marshall, J., Clément, V., Löscher, A., Meijer, Y., Brunner, D., 2019. Detectability of co_2 emission plumes of cities and power plants with the copernicus anthropogenic co_2 monitoring (co2m) mission. Atmos. Measure. Tech. Discuss. 1–35. https://doi.org/10.5194/amt-2019-180. ISSN 1867-8610.

Kuhlmann, G., Brunner, D., Broquet, G., Meijer, Y., 2020. Quantifying co_2 emissions of a city with the copernicus anthropogenic co_2 monitoring satellite mission. Atmos. Measure. Tech. Discuss. 1, 1–33. https://doi.org/10.5194/amt-2020-162. ISSN 1867-1381.

Kuhlmann, G., Henne, S., Brunner, D., Löscher, A., Meiher, Y., 2021. Smartcarb 2 – use of satellite measurements of auxiliary reactive trace gases for fossil fuel carbon dioxide emission estimation (phase 2). In: Final report of esa study contract n°4000119599/16/nl/ff/mg. URL https://www.empa.ch/documents/56101/617885/FR_Smartcarb_final_Jan2019.pdf/b456b729-90ed-42fe-b530-0aac9401666e.

Lauvaux, T., Miles, N.L., Deng, A., Richardson, S.J., Cambaliza, M.O., Davis, K.J., Gaudet, B., Gurney, K.R., Huang, J., O'Keefe, D., Song, Y., Karion, A., Oda, T., Patarasuk, R., Razlivanov, I., Sarmiento, D., Shepson, P., Sweeney, C., Turnbull, J.C., Wu, K., 2016. High-resolution atmospheric inversion of urban co_2 emissions during the dormant season of the Indianapolis flux experiment (influx). J. Geophys. Res. 121, 5213–5236. https://doi.org/10.1002/2015JD024473. ISSN 21562202.

Lei, R., Feng, S., Danjou, A., Broquet, G., Wu, D., Lin, J.C., O'Dell, C.W., Lauvaux, T., 2021. Fossil fuel co_2 emissions over metropolitan areas from space: a multi-model analysis of Oco-2 data over Lahore, Pakistan. Remote Sens. Environ. 264, 0–11. https://doi.org/10.1016/j.rse.2021.112625. ISSN 00344257.

Lian, J., Wu, L., Bréon, F.-M., Broquet, G., Vautard, R., Zaccheo, T.S., Dobler, J., Ciais, P., 2018. Evaluation of the wrf-ucm mesoscale model and ecmwf global operational forecasts over the Paris region in the prospect of tracer atmospheric transport modeling. Elementa 6. https://doi.org/10.1525/elementa.319. ISSN 23251026.

Lian, J., Bréon, F.-M., Broquet, G., Zaccheo, T.S., Dobler, J., Ramonet, M., Staufer, J., Santaren, D., Xueref-Remy, I., Ciais, P., 2019. Analysis of temporal and spatial variability of atmospheric co_2 concentration within Paris from the greenlite™ laser imaging experiment. Atmos. Chem. Phys. 19, 13809–13825. https://doi.org/10.5194/acp-19-13809-2019. ISSN 16807324.

Lian, J., Bréon, F.-M., Broquet, G., Lauvaux, T., Zheng, B., Ramonet, M., Xueref-Remy, I., Kotthaus, S., Haeffelin, M., Ciais, P., 2021. Sensitivity to the sources of uncertainties in the modeling of atmospheric co_2 concentration within and in the vicinity of Paris. Atmos. Chem. Phys. 21, 10707–10726. https://doi.org/10.5194/acp-21-10707-2021. ISSN 16807324.

Lian, J., Lauvaux, T., Utard, H., Bréon, F.M., Broquet, G., Ramonet, M., Laurent, O., Albarus, I., Cucchi, K., Ciais, P., 2022. Assessing the effectiveness of an urban co_2 monitoring network over the Paris region through the covid-19 lockdown natural experiment. Environ. Sci. Technol. 56, 2153–2162. https://doi.org/10.1021/acs.est.1c04973. ISSN 15205851.

Lian, J., Lauvaux, T., Utard, H., Bréon, F.-M., Broquet, G., Ramonet, M., Laurent, O., Albarus, I., Chariot, M., Kotthaus, S., Haeffelin, M., Sanchez, O., Perrussel, O., van der Gon, H.A.D., Dellaert, S.N.C., Ciais, P., 2023. Can we use atmospheric co_2 measurements to verify emission trends reported by cities? Lessons from a 6-year atmospheric inversion over Paris. Atmos. Chem. Phys. 23, 8823–8835. https://doi.org/10.5194/acp-23-8823-2023.

Liu, J., Fung, I., Kalnay, E., Kang, J.S., Olsen, E.T., Chen, L., 2012. Simultaneous assimilation of airs xco_2 and meteorological observations in a carbon climate model with an ensemble kalman filter. J. Geophys. Res. Atmos. 117, 1–15. https://doi.org/10.1029/2011JD016642. ISSN 01480227.

Mahadevan, P., Wofsy, S.C., Matross, D.M., Xiao, X., Dunn, A.L., Lin, J.C., Gerbig, C., Munger, J.W., Chow, V.Y., Gottlieb, E.W., 2008. A satellite-based biosphere parameterization for net ecosystem co_2 exchange: vegetation photosynthesis and respiration model (vprm). Glob. Biogeochem. Cycles 22. https://doi.org/10.1029/2006GB002735. ISSN 08866236.

Martilli, A., Clappier, A., Rotach, M.W., 2002. An urban surface exchange parametrization for mesoscale models. Bound.-Layer Meteorol. 104, 261–304 (ISSN 00068314).

Nassar, R., Napier-Linton, L., Gurney, K.R., Andres, R.J., Oda, T., Vogel, F.R., Deng, F., 2013. Improving the temporal and spatial distribution of co_2 emissions from global fossil fuel emission data sets. J. Geophys. Res. Atmos. 118, 917–933. https://doi.org/10.1029/2012JD018196. ISSN 21698996.

Nassar, R., Hill, T.G., McLinden, C.A., Wunch, D., Jones, D.B., Crisp, D., 2017. Quantifying co_2 emissions from individual power plants from space. Geophys. Res. Lett. 44, 10,045–10,053. https://doi.org/10.1002/2017GL074702. ISSN 19448007.

OCO Science Team, Gunson, M.R., Eldering, A., 2020a. Oco-2 level 2 bias-corrected xco_2 and other select fields from the full-physics retrieval aggregated as daily files, retrospective processing v10r. In: Greenbelt, MD, USA, Goddard Earth Sciences Data and Information Services Center (GES DISC). https://doi.org/10.5067/E4E140XDMPO2.

OCO Science Team, Gunson, M.R., Eldering, A., 2020b. Oco-3 level 2 bias-corrected xco_2 and other select fields from the full-physics retrieval aggregated as daily files,

retrospective processing vearlyr. In: Greenbelt, MD, USA, Goddard Earth Sciences Data and Information Services Center (GES DISC).

Oda, T., Maksyutov, S., Andres, R.J., 2018. The open-source data inventory for anthropogenic co2, version 2016 (odiac2016): a global monthly fossil fuel co_2 gridded emissions data product for tracer transport simulations and surface flux inversions. Earth Syst. Sci. Data 10, 87–107. https://doi.org/10.5194/essd-10-87-2018. ISSN 18663516.

Oda, T., Bun, R., Kinakh, V., Topylko, P., Halushchak, M., Marland, G., Lauvaux, T., Jonas, M., Maksyutov, S., Nahorski, Z., Lesiv, M., Danylo, O., Horabik-Pyzel, J., 2019. Errors and uncertainties in a gridded carbon dioxide emissions inventory. Mitig. Adapt. Strateg. Glob. Chang. 24, 1007–1050. https://doi.org/10.1007/s11027-019-09877-2. ISSN 15731596.

Pasquill, F., 1961. The estimation of the dispersion of windborne material. Meteorol. Mag. 90 (1063), 33–49.

Pillai, D., Buchwitz, M., Gerbig, C., Koch, T., Reuter, M., Bovensmann, H., Marshall, J., Burrows, J.P., 2016. Tracking city co_2 emissions from space using a high-resolution inverse modelling approach: a case study for berlin, Germany. Atmos. Chem. Phys. 16, 9591–9610. https://doi.org/10.5194/acp-16-9591-2016. ISSN 16807324.

Rayner, P.J., Michalak, A.M., Chevallier, F., 2019. Fundamentals of data assimilation applied to biogeochemistry. Atmos. Chem. Phys. 19, 13911–13932. https://doi.org/10.5194/acp-19-13911-2019. ISSN 16807324.

Reuter, M., Buchwitz, M., Schneising, O., Krautwurst, S., O'Dell, C.W., Richter, A., Bovensmann, H., Burrows, J.P., 2019. Towards monitoring localized co_2 emissions from space: co-located regional co_2 and no_2 enhancements observed by the Oco-2 and s5p satellites. Atmos. Chem. Phys. Discuss. 1–19. https://doi.org/10.5194/acp-2019-15. ISSN 1680-7324.

Santaren, D., Broquet, G., Bréon, F.-M., Chevallier, F., Siméoni, D., Ciais, P., 2020. A local to national-scale inverse modeling system to assess the potential of spaceborne colt; subgt;2lt;/subgt; measurements for the monitoring of anthropogenic emissions. Atmospheric Measurement Techniques Discussions, pages 1–41. https://doi.org/10.5194/amt-2020-138. ISSN 1867-1381.

Santaren, D., Broquet, G., Bréon, F.-M., Chevallier, F., Simeoni, D., Zheng, B., Ciais, P., 2021. A local-to national-scale inverse modeling system to assess the potential of spaceborne co_2 measurements for the monitoring of anthropogenic emissions. Atmos. Meas. Tech. 14, 403–433. https://doi.org/10.5194/amt-14-403-2021. ISSN 18678548.

Sierk, B., Fernandez, V., Bézy, J.-L., Meijer, Y., Durand, Y., Courrèges-Lacoste, G.B., Pachot, C., Löscher, A., Nett, H., Minoglou, K., Boucher, L., Windpassinger, R., Pasquet, A., Serre, D., te Hennepe, F., 2021. The copernicus co2m mission for monitoring anthropogenic carbon dioxide emissions from space. page 128. https://doi.org/10.1117/12.2599613. ISSN 1996756X.

Skamarock, W.C., Klemp, J.B., Gill, D.O., Barke, D.M., Duda, M.G., Huang, X.-Y., Wang, W., Powers, J.G., 2008. A Description of the Advanced Research Wrf Version 3.

Taszarek, M., Pilguj, N., Allen, J.T., Gensini, V., Brooks, H.E., Szuster, P., 2020. Comparison of convective parameters derived from era5 and merra2 with rawinsonde data over europe and north america. J. Clim. 1–55. https://doi.org/10.1175/jcli-d-20-0484.1. ISSN 0894-8755.

UNDESA, 2018. World Urbanization Prospects, vol. 12. ISBN 9789211483192. URL https://population.un.org/wup/Publications/Files/WUP2018-Report.pdf.

Vanderbecken, P.J., Brazidec, J.D.L., Farchi, A., Bocquet, M., Roustan, Y., Potier, Élise, Broquet, G., 2023. Accounting for meteorological biases in simulated plumes using smarter metrics. Atmos. Measure. Tech. 16 (3), 1745–1766. https://doi.org/10.5194/amt-16-1745-2023. ISSN 18678548.

Varon, D.J., Jacob, D.J., McKeever, J., Jervis, D., Durak, B.O., Xia, Y., Huang, Y., 2018. Quantifying methane point sources from fine-scale satellite observations of atmospheric methane plumes. Atmos. Meas. Tech. 11, 5673–5686. https://doi.org/10.5194/amt-11-5673-2018. ISSN 18678548.

Varon, D.J., McKeever, J., Jervis, D., Maasakkers, J.D., Pandey, S., Houweling, S., Aben, I., Scarpelli, T., Jacob, D.J., 2019. Satellite discovery of anomalously large methane point sources from oil/gas production. Geophys. Res. Lett. 11. https://doi.org/10.1029/2019GL083798. URL.

Varon, D.J., Jacob, D.J., Jervis, D., McKeever, J., 2020. Quantifying time-averaged methane emissions from individual coal mine vents with ghgsat-d satellite observations. Environ. Sci. Technol. 54, 10246–10253. https://doi.org/10.1021/acs.est.0c01213. ISSN 15205851.

Worden, R.J., Doran, G., Kulawik, S., Eldering, A., Crisp, D., Frankenberg, C., O'Dell, C., Bowman, K.W., 2017. Evaluation and attribution of oco-2 xco_2 uncertainties. Atmos. Meas. Tech. 10, 2759–2771. https://doi.org/10.5194/amt-10-2759-2017. ISSN 18678548.

Wu, L., Broquet, G., Ciais, P., Bellassen, V., Vogel, F.R., Chevallier, F., Xueref-Remy, I., Wang, Y., 2016. What would dense atmospheric observation networks bring to the quantification of city co_2 emissions? Atmos. Chem. Phys. 16, 7743–7771. https://doi.org/10.5194/acp-16-7743-2016. ISSN 16807324.

Wu, D., Lin, J.C., Fasoli, B., Oda, T., Ye, X., Lauvaux, T., Yang, E.G., Kort, E.A., 2018. A lagrangian approach towards extracting signals of urban co_2 emissions from satellite observations of atmospheric column co_2 (xco_2): X-stochastic time-inverted lagrangian transport model ("x-stilt v1"). Geosci. Model Dev. 11, 4843–4871. https://doi.org/10.5194/gmd-11-4843-2018. ISSN 1991-9603. URL https://www.geosci-model-dev.net/11/4843/2018/.

Wu, D., Lin, J.C., Oda, T., Kort, E.A., 2020. Space-based quantification of per capita co_2 emissions from cities. Environ. Res. Lett. https://doi.org/10.1088/1748-9326/ab6b35 page 13.

Wunch, D., Wennberg, P.O., Osterman, G., Fisher, B., Naylor, B., Roehl, M.C., O'Dell, C., Mandrake, L., Viatte, C., Kiel, M., Griffith, D.W., Deutscher, N.M., Velazco, V.A., Notholt, J., Warneke, T., Petri, C., Maziere, M.D., Sha, M.K., Sussmann, R., Rettinger, M., Pollard, D., Robinson, J., Morino, I., Uchino, O., Hase, F., Blumenstock, T., Feist, D.G., Arnold, S.G., Strong, K., Mendonca, J., Kivi, R., Heikkinen, P., Iraci, L., Podolske, J., Hillyard, P., Kawakami, S., Dubey, M.K., Parker, H.A., Sepulveda, E., García, O.E., Te, Y., Jeseck, P., Gunson, M.R., Crisp, D., Eldering, A., 2017. Comparisons of the orbiting carbon observatory-2 (oco-2) xco_2 measurements with tccon. Atmos. Measure. Tech. 10, 2209–2238. https://doi.org/10.5194/amt-10-2209-2017. ISSN 18678548.

Ye, X., Lauvaux, T., Kort, E.A., Oda, T., Feng, S., Lin, J.C., Yang, E.G., Dien, W., 2017. Constraining fossil fuel co_2 emissions from urban area using oco-2 observations of total column co2. Atmos. Chem. Phys. https://doi.org/10.5194/acp-2017-1022.

Ye, X., Lauvaux, T., Kort, E.A., Oda, T., Feng, S., Lin, J.C., Yang, E.G., Wu, D., 2020. Constraining fossil fuel co_2 emissions from urban area using oco-2 observations of total column co2. J. Geophys. Res. Atmos. 125, 1–29. https://doi.org/10.1029/2019JD030528. ISSN 21698996.

Zheng, B., Chevallier, F., Ciais, P., Broquet, G., Wang, Y., Lian, J., Zhao, Y., 2020. Observing carbon dioxide emissions over china's cities with the orbiting carbon observatory-2. Atmos. Chem. Phys. 1–17. https://doi.org/10.5194/acp-2020-123. ISSN 1680-7316.